MATERIALS CHEMISTRY
FRONTIERS

RESEARCH ARTICLE

View Article Online
View Journal

Cite this: DOI: 10.1039/d6qm00036c

Vacuum-responsive and water-soluble lanthanide(III)/2-oxonicotinate coordination polymers with high photoluminescence efficiency

Maialen Terceño-Carrillo,[a] Laura Razquin-Bobillo,[a] Sergio Carrasco,[b] Patricia Horcajada,[b] Garikoitz Beobide,[c] Jose Angel García,[d] Pablo Salcedo-Abraira,[e] Andoni Zabala-Lekuona,[a] Antonio Rodríguez-Diéguez[e] and Javier Cepeda *[a]

In this work, we report on the structural and physicochemical characterization and an in-depth photophysical study of a family of isostructural coordination polymers (CPs) with the general formula $\{[M_2(\mu_3\text{-2onic})_4(H_2O)_4](ClO_4)_2\cdot 2H_2O\}_n$ (where M(III) = Y (**1**$_{Y}$), Nd (**2**$_{Nd}$), Eu (**3**$_{Eu}$), Gd (**4**$_{Gd}$), Tb (**5**$_{Tb}$), Dy (**6**$_{Dy}$), Er (**7**$_{Er}$) and Yb (**8**$_{Yb}$) and 2onic = 2-oxonicotinate). They consist of a cationic 2D layered structure in which two eight-coordinated rare-earth centres are interconnected by means of 2onic ligands, which demonstrates great flexibility with respect to changes in temperature and pressure (vacuum) derived from partial dehydration implying both lattice and coordination water molecules, which in turn promotes the rearrangement of the hydrogen-bonded network. Similar structural breathing effects are observed under variable gas-pressurization conditions, leading to some metastable phases while vacuum conditions are maintained. Periodic density functional theory (PDFT) calculations performed on **1**$_{Y}$ with variable amounts of water successfully reproduced the structural evolution during dehydration. The fact that the vacuum-/pressure-induced effect is fully reversible in addition to the significantly improved photoluminescence (PL) shown by the vacuum-/pressure-activated compounds shifts the attention towards these compounds as potential pressure and humidity sensors. **2**$_{Nd}$ and **8**$_{Yb}$, in addition to acting as emitters in the visible range, behave as near-infrared (NIR) emitters, with the former displaying characteristic emission even at room temperature. A thorough analysis of the excitations and energy-transfers by means of semi-empirical methods and multi-configurational calculations on suitable fragment models, and further confirmation by density of states (DOS) theory on the PDFT-optimized structure, allows elucidating the PL mechanism operating in the variable emission in the solid state. The water solubility of the compounds allows the study of the PL properties of the complexes, which surprisingly present quantum efficiencies exceeding those of the solid state especially in the solution of **5**$_{Tb}$ (with the quantum yield (QY) increased from 1.6 to 21.5%).

Received 16th January 2026,
Accepted 3rd February 2026

DOI: 10.1039/d6qm00036c

rsc.li/frontiers-materials

Introduction

During the last few decades, coordination polymers (CPs) consisting of lanthanide ions (Lns), hereafter LnCPs, have received huge attention from synthetic researchers due to their intriguing photoluminescence (PL) properties arising from their characteristic valence 4f subshell, which endow these compounds with characteristic narrow-band and highly pure coloured emissions in a wide spectrum covering both the near-infrared and, mainly, the visible range.[1–3] In fact, these unique features have enabled LnCPs to bring important advancements in many applications related to a wide variety of disciplines such as biomedicine,[4–6] optical imaging,[7,8] anticounterfeiting[9–11] and many other disciplines related to lighting materials[12–14] owing to their bright and long-lived luminescence signal. Notwithstanding the indispensable role of Ln, the low extinction coefficient of their intra-Ln f–f absorption bands makes LnCPs also require adequate ligands with the ability to efficiently sensitize their emission, *i.e.* transferring energy to their excited states by means of the antenna

---

[a] *Departamento de Química Aplicada, Facultad de Química, University of the Basque Country (EHU), 20018 Donostia-San Sebastián, Spain. E-mail: javier.cepeda@ehu.eus*

[b] *Advanced Porous Materials Unit (APMU), IMDEA Energy Institute, Avda. Ramón de la Sagra 3, E-28935, Móstoles, Madrid, Spain*

[c] *Departamento de Química Orgánica e Inorgánica, Facultad de Ciencia y Tecnología, University of the Basque Country (EHU), 48940, Leioa, Spain*

[d] *Departamento de Física, Facultad de Ciencia y Tecnología, University of the Basque Country (EHU), 48940, Leioa, Spain*

[e] *Departamento de Química Inorgánica, Facultad de Ciencias, Universidad de Granada, Av. Fuentenueva S/N, 18071 Granada, Spain*

effect, to eventually show high quantum yield (QY) and stability when employed in various applications.[2] In this sense, ligands containing β-O,O′ moieties have been shown to act as good sensitizers when they are characterized by the following features: (i) they consist of a conjugated π–π system promoting intense light absorption, (ii) they can form strong bonds with Ln giving rise to chelating rings, which affords stability to the complex and favours the antenna effect, and (iii) their electronic structure allows efficient intersystem crossing to populate a low-lying excited triplet state (T_1).[15,16] For instance, so-called β-diketones have been largely explored given their excellent capacity to yield brightly emitting complexes,[17] which are acknowledged for their fascinating photophysical features and high stability in many media. This explains why they have found large applicability not only in the solid state (UV dosimeters, solar concentrators and so on)[18] but also in solution (biological probes, inks).[19] However, many of these molecules act as terminal ligands and fail to link Lns into CPs even if they are combined with other ancillary ligands,[20] thus often limiting the potential multifunctional character of the compound when it comes to the interplay between PL and structural dynamic response to external stimuli such as temperature or pressure.[21] In contrast, LnCPs suffer from stability issues, especially in water solutions, where most of the examples are either completely insoluble or fully decompose into other species lacking the original properties, hence making their processing difficult as non-toxic inks and probes in biological systems or their printing into smart devices.[1,22,23] Therefore, finding materials that maintain equilibria between structural flexibility in the solid state and dissolving capacity in water in addition to having stability in all media is very challenging.

Coming back to the field of sensing, luminescent LnCPs deserve a special mention given their good performance as chemical and physical sensors,[24–26] among which the former have been largely revisited during the last few years[27–29] whereas the latter remain comparatively less studied and mainly limited to thermometers.[25] Thus, other relevant application fields such as luminescence-based pressure-/vacuum-sensing still remain nowadays practically unexplored, with most of the examples referring to O_2 sensors.[30] In this context, CPs exhibit ordered but "soft" structures, with strong coordination bonds complemented by weaker interactions, particularly involving lattice crystallization solvents or ionic species. Such molecular arrangement may happen to imbue the solid with a particular sensitivity towards small changes occurring in the environment, which can generate a luminescence response. This is why, notwithstanding the fact that O_2 is a major component of ambient air, sensing of vacuum under other atmospheric conditions could be equally interesting.

In our quest of finding novel metal–organic materials presenting good PL properties and considering all the previously mentioned ideas, in the present work we have focused on the photophysical characterization of a family of isostructural CPs based on the 2-oxonicotinate (2onic) ligand. This ligand, similar to the previously explored methylated derivative 6-methyl-2-oxonicotinate (6m2onic),[31,32] keeps the capacity to establish stable six-membered chelating rings with Lns that allows for providing Ln-centred emission in both solid state and aqueous solution while it also extends the coordination and polymerization. More interestingly, yet the PL properties are comparatively worse for 2onic-based compounds with respect to 6m2onic, and the layered and ionic framework of the former endows the herein described compounds with intriguing variable luminescence that derives from vacuum-/pressure-triggered subtle structural rearrangement mediated by partial dehydration. In this sense, concise characterization supported by both a broad set of experiments and DFT computation allows unraveling framework-level structural mechanisms leading to modulation of PL properties of these materials and their potential sensing of slight physical changes under ambient conditions.

Results and discussion

Structural description of $\{[M_2(\mu_3\text{-2onic})_4(H_2O)_4](ClO_4)_2\cdot 2H_2O\}_n$ [where M(III) = Y (1_{Y}), Nd (2_{Nd}), Eu (3_{Eu}), Gd (4_{Gd}), Tb (5_{Tb}), Dy (6_{Dy}), Er (7_{Er}) and Yb (8_{Yb})]

All these compounds are isostructural according to their similar powder X-ray diffraction (PXRD) patterns (Fig. S4–S11) and crystallize in the *P*2/*n* space group (or *P*2/*c* alternate setting of space group no. 13) in the form of a 2D layered structure, which resembles those previously reported by Liao *et al.*,[33,34] in spite of the remarkable differences (for instance, the *c* parameter differs by *ca.* 1 Å and the *β* angle by more than 10° for the Gd counterpart) caused by the high flexibility of the framework. Taking compound 5_{Tb} as a reference, the asymmetric unit is composed of two halves of crystallographically independent Tb(III) atoms (because they lie on binary axes), two 2onic ligand copies, two coordination water molecules, a perchlorate anion and a lattice water molecule (Fig. 1). Both Tb(III) atoms, located on a binary axis, are octa-coordinated but they display different environments. The coordination polyhedron around the Tb1 atom is best described by a triangular dodecahedron (as confirmed by continuous shape measures, S_{TDD} = 0.437, Table S4) formed by four carboxylate oxygen atoms, each of them belonging to the 2onic ligand, in addition to four coordination water

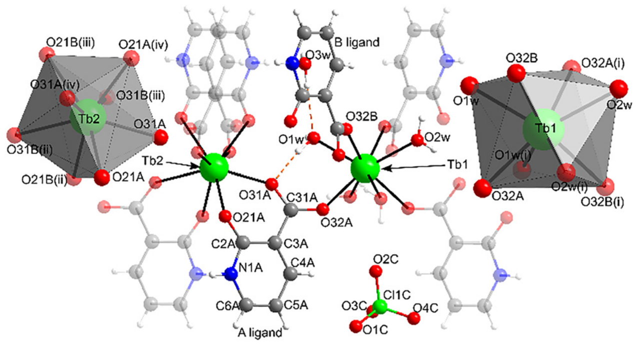

Fig. 1 View of the coordination fragment of 5_{Tb} showing the environment around both Tb(III) atoms and lattice molecules. Atoms pertaining to the asymmetric unit are shown in bold colour whereas their copies are shown with high transparency. Coordination polyhedra with the numbering scheme are also presented. Colour coding: carbon (grey), hydrogen (white), nitrogen (blue), oxygen (red) and terbium (green).

Table 1 Selected bond lengths for compound $\mathbf{5_{Tb}}$[a] (Å)

Coordination sphere of the Tb1 atom			
Tb1–O1w	2.470(3)	Tb1–O32A	2.326(3)
Tb1–O1w(i)	2.470(3)	Tb1-O32A(i)	2.326(3)
Tb1–O32B	2.321(3)	Tb1–O2w	2.488(3)
Tb1–O32B(i)	2.321(3)	Tb1–O2w(i)	2.488(3)
Coordination sphere of the Tb2 atom			
Tb2–O21A	2.367(3)	Tb2–O21B(ii)	2.382(3)
Tb2–O31A	2.338(3)	Tb2–O31B(ii)	2.347(3)
Tb2–O21A(iv)	2.367(3)	Tb2–O21B(iii)	2.382(3)
Tb2–O31A(iv)	2.338(3)	Tb2–O31B(iii)	2.347(3)

[a] Symmetries: (i) $1/2 - x, y, 1/2 - z$; (ii) $3/2 - x, -1 + y, 1/2 - z$; (iii) $x, -1 + y, z$; (iv) $3/2 - x, y, 1/2 - z$.

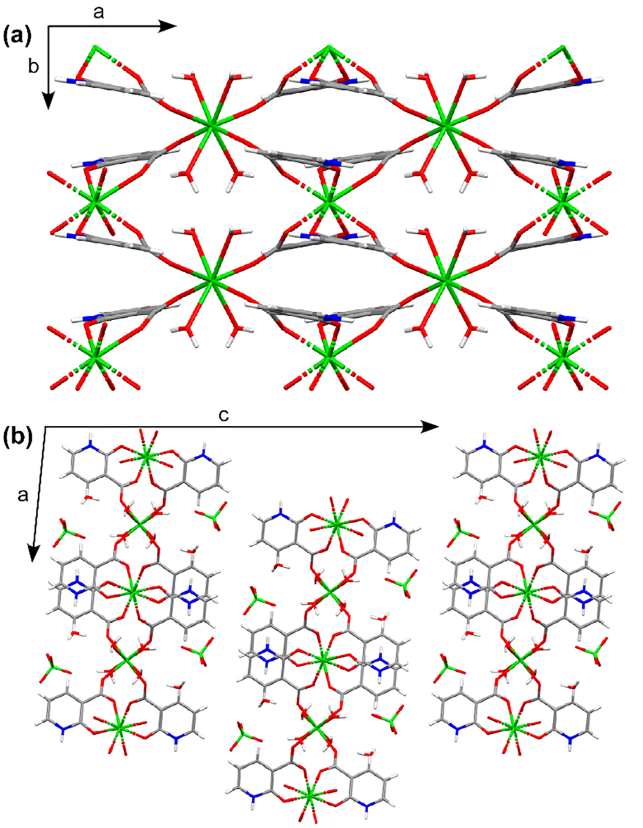

Fig. 2 (a) View of the 2D layer of compound $\mathbf{5_{Tb}}$ along the *c* axis showing the tetragonal plane network. Note that perchlorate and water molecules are omitted for clarity. (b) Packing of the structure showing the piling of the layers.

molecules. On the other hand, the polyhedron of the Tb2 atom is formed by four chelating O21(ketone)/O31(carboxylate)-based moieties, resembling a square antiprism (S_{SAPR} = 0.864), similar to those found in compounds based on a derivative of the ligand.[35] In any case, it is worth noting the systematically longer bond distances observed for the water-based oxygen atoms than for the rest of oxygen atoms (Table 1). This fact, together with higher coordination flexibility of the former bonds, is probably the reason for the lower distortion of the coordination of Tb1 with respect to the ideal polyhedron.

The two independent ligands present the same μ-κ^2*O21,O31*:κ*O32* coordination pattern, based on the chelating ring around the Tb2 atom and the monodentate linkage with the Tb1 atom. To acquire such a binding mode, the carboxylate group needs to be twisted out of the aromatic mean plane, where the rotation angle is slightly higher for the B ligand (of 27.8°) compared to the A ligand (26.2°). In this way, the ligands bridge both coordination centres with each other, in such a way that each of the four non-chelating carboxylate oxygen atoms (of 2onic ligands) arising from the Tb2 centre is linked to a Tb1 centre, imposing Tb···Tb distances of *ca.* 5.90 (for the A ligand) and 5.95 Å (for the B ligand). As a result, the coordination between these two centres takes place along two directions in such a way that layers show rhombic rings in the form of a tetragonal plane network with the **sql** topology and $(4^4 \cdot 6^2)$ point symbol (Fig. 2a). Within the layers, the coordinated water molecules use one of their hydrogen atoms to establish strong hydrogen-bonding interactions with the chelating carboxylate oxygen atoms. From this point on, the second hydrogen atom of the water molecules interacts differently, since it is involved in an intralayer hydrogen bond with a neighbouring coordinated water molecule in the case of O1w whereas that of O2w is directed towards one of the oxygen atoms of the perchlorate anion. Moreover, the arrangement of the ligands pending from both centres is that in which neighbouring aromatic rings get close and parallel to each other to maximise π–π interactions. In particular, remarkable interactions are found between adjacent A and B ligands pertaining to the Tb2 centre and between copies of those ligands pending from both Tb1 and Tb2 centres, in such a way that stacking interactions are observed along the crystallographic *b* axis. In addition to these interactions, the lattice water molecule is also involved in hydrogen bonds with perchlorate and coordinated water molecules, somehow reinforcing the internal cohesion of the layers. However, none of the aforementioned major interactions are involved in the connectivity between adjacent layers, resulting in weak interlayer packaging, with the layers stacked along the *c* axis by means of weak interactions involving perchlorate anions (Fig. 2b). This fact seems to indicate that the packing of the structure could present remarkable flexibility, which agrees with the structural polymorphism found for these compounds (similarity to other previously published compounds).

Framework response dynamics to temperature and variable pressure

Inspired by the potentially flexible framework of these compounds, consisting of a 2D-layered structure weakly bonded by ClO_4^- anions and lattice H_2O molecules, their structural evolution was studied according to both temperature and vacuum/pressure. To start with, routine thermogravimetric analysis (TGA) conducted on a fresh sample of compound $\mathbf{3_{Eu}}$ revealed a two-step dehydration scheme (see Fig. S1 and Table S2 in the S2 section of the SI for further details): (i) first, partial dehydration (PD) in which both the lattice and two coordination water molecules are lost (within 105–165 °C), which yields $\{[Eu_2(2onic)_4(H_2O)_2](ClO_4)_2\}_n$ (hereafter $\mathbf{3_{Eu}}$-PD), and (ii) second, loss of the remaining coordination water molecules (within 165–205 °C), leading to the fully dehydrated (FD) compound $\{[Eu_2(2onic)_4](ClO_4)_2\}_n$ (hereafter $\mathbf{3_{Eu}}$-FD). Despite the fact that $\mathbf{3_{Eu}}$-FD presents chemical stability in the 205–305 °C range (a plateau in the TG curve), a parallel thermodiffractometric experiment (Fig. S2) confirmed that the compound becomes amorphous above 130 °C, that is, before the first dehydration step is completed (according to TGA data). Therefore, no reliable conclusions can be drawn from the fitting of these PXRD data, which significantly limits the potential applicability of the properties of the resulting high-temperature products.

On this basis and considering the limited diffraction capacity of these compounds under heating, softer dehydration conditions were followed to approach the potential dynamics of the framework forced by their controlled dehydration. Accordingly, the evolution of PXRD data for $\mathbf{7_{Er}}$ was followed under high vacuum. As the sample was slightly depressurized from an open atmosphere (OA) down to low pressure (achieving $4.6 \cdot 10^{-6}$ mbar at the end of the experiment), a slight shifting of *ca.* 0.1° was observed in many diffraction maxima (Fig. 3).

In parallel, the mass loss occurring for the compounds was studied by gravimetry during exposure of a representative sample to high vacuum (of *ca.* 10^{-5} mbar) in an outgassing station (see details in the S7 section of the SI), finding that this process forces the release of not only the lattice but also two of the coordination water molecules (4 H_2O accounting for an experimental loss of 6.82% that fits well with the theoretical loss of 6.27%, see Table S5 in the S7 section of the SI), thus leading to the aforementioned compound $\mathbf{7_{Er}}$-PD. Pattern-matching analyses on selected diffractograms showed slight contraction of the unit cell during the initial pressurization stage although it turns into drastic eventual cell expansion under high vacuum for several hours (Table 2). In particular, it is seen that the partial dehydration (loss of 4 H_2O molecules) slightly shortens the crystallographic *a* and *c* parameters while it lengthens the *b* parameter and also closes the *β* angle. Interestingly, exposure of the sample to air for some hours reverted the process back to the pristine material, as evidenced by PXRD pattern comparison, suggesting spontaneous water uptake from atmospheric moisture under open-air conditions.

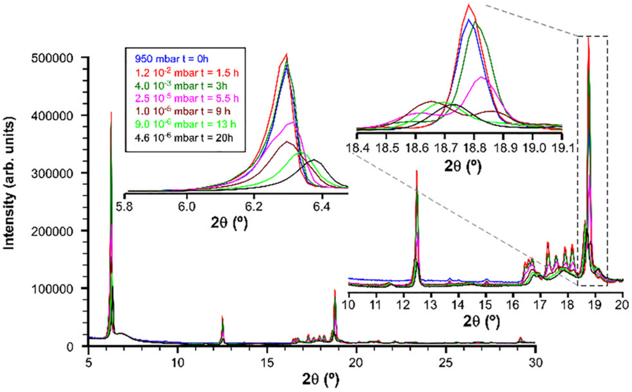

Fig. 3 Evolution of the PXRD data of compound $\mathbf{7_{Er}}$ under progressive vacuum pressurization. The insets show augmented regions where key shifting of diffraction maxima occurs.

Table 2 Experimental and periodic DFT-computed structural data at variable-vacuum/dehydration stages of these compounds[a]

	Cell parameters					
Comp.	*a* (Å)	*b* (Å)	*c* (Å)	*β* (°)	*V* (Å^3)	Δ*V* (%)
Experimental X-ray structure						
$\mathbf{7_{Er}}$-**OA**	10.11	6.40	28.55	95.57	1838.6	—
$\mathbf{7_{Er}}$-$\mathbf{10^{-3}}$	10.11	6.39	28.49	95.47	1832.2	−0.34
$\mathbf{7_{Er}}$-$\mathbf{10^{-5}}$	10.09	6.37	28.45	95.45	1820.3	−1.00
$\mathbf{7_{Er}}$-$\mathbf{10^{-6}}$	10.03	6.58	28.28	95.29	1858.5	+1.08
PBC-simulated structures						
$\mathbf{1_Y}$	9.91	6.82	28.95	95.95	1944.1	—
$\mathbf{1_Y}$-**WL**[a]	9.96	6.67	28.85	96.17	1905.9	−1.96
$\mathbf{1_Y}$-**PD**	9.67	6.94	28.72	94.28	1925.8	−0.94
$\mathbf{1_Y}$-**FD**	9.59	6.96	28.63	95.38	1902.5	−2.14

[a] Labels employed for the structures simulated under periodic boundary conditions refer to several progressive dehydration steps: (i) compound $\mathbf{1_Y}$ without lattice molecules ($\mathbf{1_Y}$-**WL**: $\{[Y_2(2onic)_4(H_2O)_4](ClO_4)_2\}_n$); (ii) the partially dehydrated compound without lattice and two coordination water molecules ($\mathbf{1_Y}$-**PD**: $\{[Y_2(2onic)_4(H_2O)_2](ClO_4)_2\}_n$) and (iii) the fully dehydrated compound ($\mathbf{1_Y}$-**FD**: $\{[Y_2(2onic)_4](ClO_4)_2\}_n$).

In order to shed some light on the possible structural transformation taking place during the vacuum-triggered partial dehydration, DFT calculations were performed on the crystal structure of compound $\mathbf{1_Y}$ with the CASTEP code of Materials Studio[36] under periodic boundary conditions (PBC, hereafter PDFT) given its lighter electronic structure compared to the rest of lanthanide-based counterparts. In an attempt to correlate the water release steps with unit cell parameter evolution, several structures representing all possible dehydration stages (structure without lattice water: WL, partially dehydrated without lattice and half of coordination molecules: PD and fully dehydrated: FD; see footnote in Table 2 for detailed explanation) were optimized allowing unit cell parameters to be slightly adapted. As observed in Table 2, the main experimental evolution of the lattice parameters (shortened *a*, *c* and *β* parameters and lengthened *b* parameter) and the eventual unit cell volume increase after prolonged vacuum (from 1820.3 to 1858.5 Å^3) are both well reproduced for the simulated structures but only up to the data of compound $\mathbf{1_Y}$-**PD** (for which a slight relative cell volume increase from 1905.9 for $\mathbf{1_Y}$-**WL** to 1925.8 Å^3 for $\mathbf{1_Y}$-**PD** takes place during the loss of two coordination water molecules). Thus, the similar trend found in the simulated data supports the experimental loss of 4 water molecules (2 crystallization and 2 coordination molecules) and confirms the structural stability and flexibility of the compound even after the loss of coordination water molecules in the Y1 atom and despite the weak interactions dominating the 2D-layered structure. In any case, these non-innocent dehydration dynamics bring important consequences in the coordination environment of both metal atoms, mainly for the Y1 centre in which the reduction of the coordination index from 8 to 6 is accompanied of a substantial decrease in the polyhedron symmetry (from less distorted triangular dodecahedron symmetry (S_{TDD} = 0.453) to a highly distorted pseudo-octahedron (S_{OC} = 1.744)). Therefore, as it will be detailed later in the manuscript, significant changes are expected to occur in the properties of these compounds in view of changes occurring in the chromophore.

To further investigate the structural response under external *stimuli*, a series of variable-pressure powder X-ray diffraction (VP-PXRD) experiments using different gas loadings were performed at 25 °C on compound $\mathbf{3_{Eu}}$. The first test consisted in several cycles of vacuum-pressurization (Fig. 4). Upon the first vacuum cycle (red), significant shifts of the diffraction peaks were observed. The initial diffractogram displayed a broad reflection that resolved into three contributions centered at 6.27, 6.19, and 6.10° (2*θ*). Application of vacuum enhanced the 6.27° reflection at the expense of the lower-angle components, whereas restoring atmospheric pressure (blue) partially recovered their relative intensities, reproducing the high-vacuum data collected for $\mathbf{7_{Er}}$. Consistent with other flexible Ln-MOFs, evacuation triggered partial desolvation, and a PXRD-detectable structural rearrangement that can be reversed upon exposure to air was observed, in line with soft-porous-crystal behavior.[37,38] However, the initial pattern was not fully re-established during the experiment, since additional peak splitting at higher angles persisted (*e.g.*, >18° (2*θ*)). Subsequent pressurization with air up to 1.6 bar (green) irreversibly stabilized the 6.27° reflection, while the lower-angle contributions could no longer be recovered during the experiment. After completing a full vacuum/air-pressure cycle, the diffractogram showed enhanced intensities but no further changes in peak positions, indicating that the vacuum-induced rearrangement had become locked for, at least, $P < 2$ bar. Following evacuation, subsequent pressurization seems to lock the framework in a metastable configuration, reminiscent of adsorption-driven hysteresis reported for breathing MOFs.[39,40] This behavior is concordant with slow rehydration kinetics occurring in the compound that is associated with its non-porous structure and, thus, expected low gas water capture capacity from ambient moisture and subsequent diffusion of water molecules within the particles.[41]

In contrast, in the second test, samples were directly pressurized up to 1.6–1.7 bar with either air or argon, never below 1 bar and without applying vacuum, exhibiting no significant structural modifications compared to the pristine diffractogram (Fig. 5). Only global intensity changes were detected. Hence, vacuum appeared as the main driving force behind the structural rearrangement observed in Fig. 4, whereas moderate compression alone did not promote any phase evolution within the accessible pressure window, which agrees with previous studies where MOF transitions are typically observed under much higher hydrostatic loads.[42] Whether higher Ar/air pressures would induce further transformations remains uncertain because achieving higher pressures lies beyond the operational limits of the *in situ* setup.

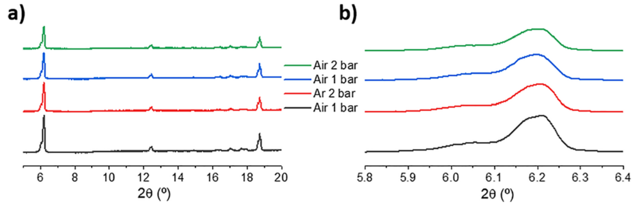

Fig. 5 (a) PXRD patterns of $\mathbf{3_{Eu}}$ upon consecutive *in situ* pressurization–depressurization cycles (from bottom to top); (b) amplification of the region 5.8–6.4° (2*θ*). No peak shifting was observed.

In order to shed some light on this behavior, additional CO_2 pressure experiments were conducted at 10 bar for 16 h on the samples used in the previous experiments. Interestingly, the sample from the first test (vacuum-pressurization) displayed a transient beige/pinkish color to the naked eye immediately after recovering the material from the reactor, although it reverted to its original white appearance within minutes under ambient conditions (Fig. S13). PXRD patterns revealed small yet measurable variations in the main low-angle reflection. For the sample from the first test (vacuum-pressurization; Fig. 6a), the peak shifted from 6.27 to 6.23° (2*θ*), consistent with a lattice expansion of ∼0.05 Å (interplanar distance, *d*). Conversely, the sample from the second test (pressurization-depressurization without vacuum, Fig. 6b) showed a shift from 6.21 to 6.23° (2*θ*), corresponding to a slight contraction of ∼0.03 Å (*d*). Remarkably, both cases converged to a common equilibrium value of 6.23° (2*θ*), suggesting that exposure to CO_2 promotes structural relaxation towards a similar metastable configuration regardless of the sample history, in agreement with CO_2-induced breathing observed by *in situ* PXRD in other flexible MOFs.[43,44] In any case, further PXRD analysis of the aerated sample confirmed the reversibility of the process back to the original compound (Fig. S14). Taken together, these findings reinforce the notion that the framework can explore

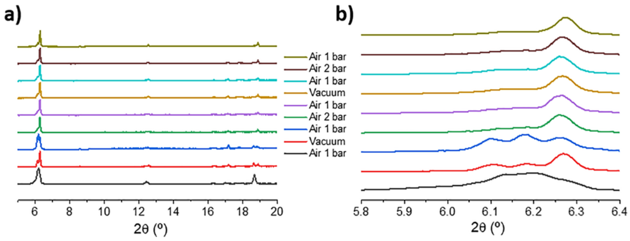

Fig. 4 (a) PXRD patterns of $\mathbf{3_{Eu}}$ upon consecutive *in situ* vacuum-pressurization cycles (from bottom to top); (b) amplification of the region 5.8–6.4° (2*θ*).

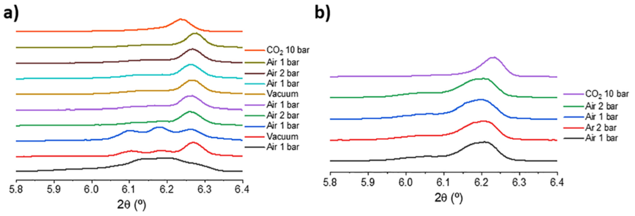

Fig. 6 PXRD patterns of $\mathbf{3_{Eu}}$ after 16 h at 10 bar CO_2 previously used in the (a) vacuum-pressurization test; (b) pressurization-depressurization test.

multiple metastable configurations depending on the applied *stimulus*, thus supporting its potential as a responsive material for luminescence-based sensing.

Photophysical study of the excited states by means of UV-Vis absorption and photoluminescence spectroscopy

The solid state UV-Vis absorption spectra of all compounds, measured in the solid state, show a similar pattern that consists of a main band peaking at *ca.* 335 nm, followed by a shoulder of an overlapped band at *ca.* 305 nm and a less intense noisy band with its maximum at around 245 nm (see Fig. 7 and Fig. S15). These patterns resemble that of the free H2onic ligand, meaning that these bands can be unequivocally assigned to ligand absorptions, although a slight hypsochromic shift associated to the coordination of 2onic to Ln ions, mainly for the dominant band, is appreciated for the compounds. It is worth mentioning that the spectra of compounds $\mathbf{3_{Eu}}$, $\mathbf{5_{Tb}}$ and $\mathbf{6_{Dy}}$ display some weak and narrow bands attributed to the intraionic f–f transitions of the corresponding lanthanides. Multiconfigurational random phase approximation (MC-RPA) calculations (see the Computational details section) were performed on appropriate models (optimized at the DFT level) of both the free H2onic ligand and compound $\mathbf{4_{Gd}}$, which allow both reproducing well the experimental spectra and confirming the π–π^* ligand-centred (LC) nature of the excitations (Fig. 7 and Fig. S94, S95 and Table S7). Moreover, the possible occurrence of ligand-to-metal charge transfer (LMCT) transitions in the absorption region covering the bands was ruled out given that these sorts of transitions involve energies above the experimental spectral window (of *ca.* 55000 cm^{-1} and thus below 182 nm in the spectrum, see Fig. S96). Taking the absorption maxima found in the solid state absorption spectrum of $\mathbf{4_{Gd}}$, the lowest-energy singlet excited states of these Ln-CPs can be estimated at *ca.* 29850 and 32260 cm^{-1} (335 and 310 nm, see Fig. 7), attributed to the S_1 and S_3 excited states (S_1 and S_2 hereafter for convenience). A similar estimation for the H2onic ligand sites the S_1 state at *ca.* 28570 cm^{-1} (according to the maximum at 350 nm, see Fig. S95). Reasonably close values are found according to the vertical excitations and band maxima of the calculated spectra (Table 3). In addition, the zero-phonon lines (ZPL) for the first excited singlet states could be lying at about 26315 and 26595 cm^{-1}, respectively, for the H2onic ligand and compound $\mathbf{4_{Gd}}$, based on the absorption borders of experimental UV-Vis spectra (Table 3).

Once the energies of the excited singlet states were known, we continued studying the PL properties of these samples at variable temperature in order to locate the lowest-lying excited triplet state given its potential implication in the PL mechanism of these Ln-CPs. Under UV light of 365 nm, a polycrystalline sample of H2onic displays brilliant blue emission whereas the sample of compound $\mathbf{4_{Gd}}$ emits blue-violet light as observed in the micro-PL images (Fig. 8). Accordingly, the emission spectrum collected under laser excitation (λ_{ex} = 325 nm) of the Gd-based compound is dominated by a band peaking at 395 nm attributed to the ligand's emission given that Gd(III) lacks intraionic electronic transitions in that region of the spectrum.[45] This band is slightly red-shifted compared to that shown by the free H2onic ligand measured with the same experimental setup (λ_{em} = 405 nm), which is associated to the coordination of the ligand in the structure of $\mathbf{4_{Gd}}$. This fact is also translated into a much shorter Stokes shift, of less than 10 nm in $\mathbf{4_{Gd}}$ while it is of 40 nm in H2onic. Moreover, the H2onic ligand's emission band is also remarkable for its wideness compared to that of $\mathbf{4_{Gd}}$, seeming to be composed of a second less intense band peaking at *ca.* 440 nm. The analysis of the decay curves measured at both wavelengths by means of a LED-based pulsed source reveals that both contributions arise

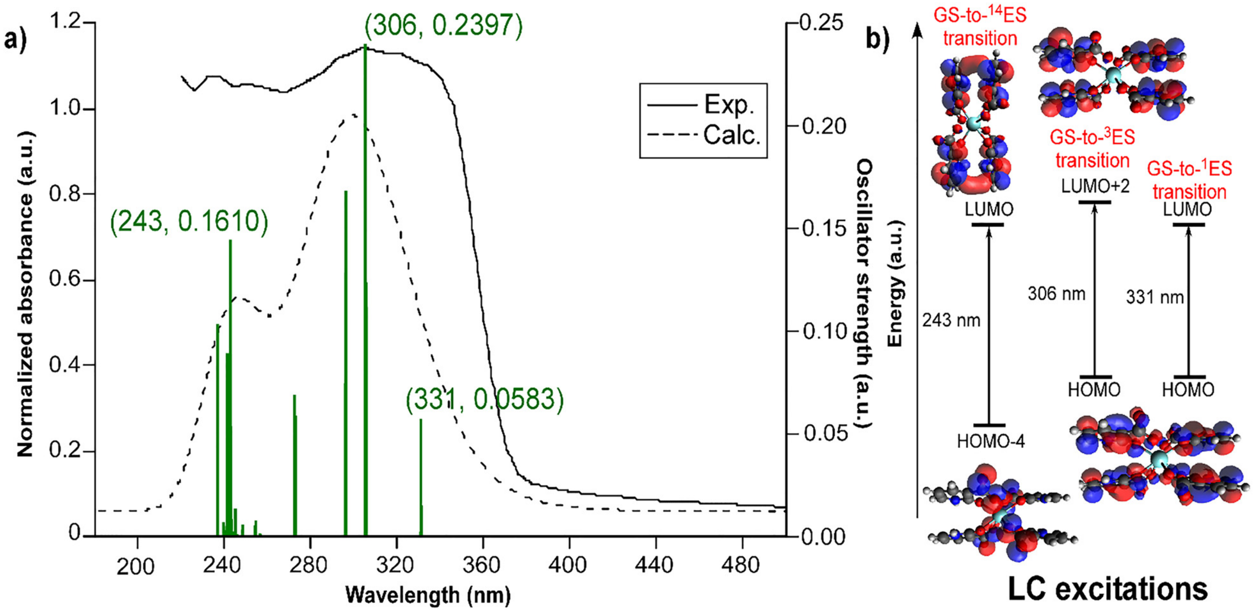

Fig. 7 (a) Experimental and calculated absorption spectra of compound $\mathbf{4_{Gd}}$ in the solid state at RT. (b) Schematic diagram of the main electronic transitions giving rise to excited S_1 (S_1), S_2 (S_3) and S_3 (S_{14}) states.

Table 3 Experimentally estimated and computed energies for the lowest-lying states of interest for the H2onic ligand and compound $\mathbf{4_{Gd}}$[a]

	ZPL		E_S (cm^{-1})		E_T (cm^{-1})	
Comp.	S_1	T_1	Exp.	Calc.	Exp.	Calc.
Ligand	26 315	22 200	28 570	30 490	20 033	19 125
$\mathbf{4_{Gd}}$	26 595	22 860	29 850	30 210	19 160	18 570

[a] The experimental energy values for the singlet and triplet states are estimated from the UV-Vis absorption and TRES measurements, respectively. The calculated energy values are obtained from MC-RPA methodology for both H2onic ligand and $\mathbf{4_{Gd}}$.

from the same electronic level (vibronic progression) given their similar emission lifetime (τ_{av} = 5.39 ns at λ_{em} = 400 nm and τ_{av} = 5.32 ns at λ_{em} = 440 nm, Fig. S18). No such equivalent signal could be measured at RT for compound $\mathbf{4_{Gd}}$ due to its both low intensity and shorter lifetime. Given the impossibility of finding phosphorescence emissions which could clarify the energy of excited triplet states, the measurements were repeated at 25 K. To start with H2onic, both the excitation and emission bands are notoriously narrowed, while the emission band is also red-shifted from 400 to 440 nm (being aligned to the RT shoulder, see Fig. S19). Interestingly, although the band maximum maintains a fluorescence signal (increased to τ_{av} = 7.84 ns at λ_{em} = 440 nm), the band shoulder clearly represents a phosphorescence emission owing to its long-lived component (τ_{av} = 71.4 ms at λ_{em} = 475 nm, Fig. S20). Such a long lifetime lasting in the range of a few milliseconds suggests that the signal is being emitted from a ligand-centred excited triplet state. A similar effect is observed for compound $\mathbf{4_{Gd}}$ at low temperature, while the emission spectrum also reveals a second broad band centred at *ca.* 500 nm (Fig. S21) that is attributed to the phosphorescence emission under steady-state irradiation, as supported by its lifetime (τ_{av} = 6.4 ms, see Fig. S22). It is also worth noting that the first (main) band of the emission spectrum of $\mathbf{4_{Gd}}$ presents a slightly shorter lifetime than the free ligand (τ_{av} = 0.84 ns at λ_{em} = 395 nm), which may be due to a more effective intersystem crossing in the compound caused by both the reduction of the vibrational component in the CP as observed in previous works[31] and the occurrence of the heavy atom effect caused by Gd(III).[46] With the aim of isolating the delayed band corresponding to the triplet state emission, time-resolved emission spectra (TRES) were measured at low temperature for both samples and, gathering the data at t = 3 ms the corresponding phosphorescence spectra were constructed (Fig. S23). Both samples exhibit wide bands peaking at *ca.* 500 nm in good agreement with the previous measurements. After processing these bands in energy scale and using appropriate fittings (Fig. S24 and S25), the barycentre and zero-phonon energy of the excited triplet state manifold were estimated (Table 3). The results for the triplet barycentre of both compounds are concordant with those values estimated *via* the vertical excitation method, by which the triplet state energy is calculated as ($E_T - E_S$) for the models (the H2onic ligand molecule or the suitable complex model for $\mathbf{4_{Gd}}$) optimized at the triplet state geometry (19125 cm^{-1} for H2onic and 18570 cm^{-1} for $\mathbf{4_{Gd}}$).

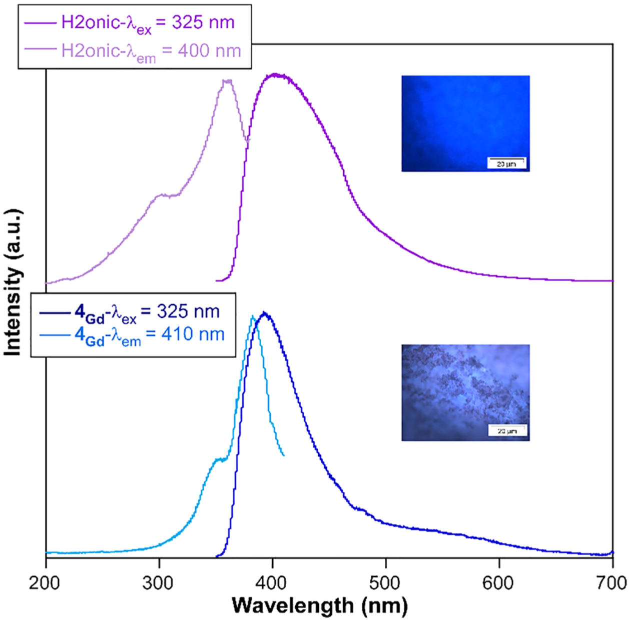

Fig. 8 Excitation and emission spectra of the free H2onic ligand and compound $\mathbf{4_{Gd}}$ recorded at RT under an open atmosphere. The inset shows micro-photographs of the powdered samples taken under UV illumination (λ_{ex} = 365 nm). Note that the excitation spectrum for $\mathbf{4_{Gd}}$ was recorded by fixing the emission wavelength above the emission band maximum in order to properly record the whole excitation band.

To end up with this section, it must be emphasized that the photophysical properties of these compounds were also computed on the PDFT-optimized structure of $\mathbf{1_Y}$ for comparative purposes and to validate the conclusions previously derived from representative fragment models. As observed in Fig. S16 in the SI, though the present computations somewhat underestimate the band gap compared to the experimental measurements (2.79 *vs.* 3.18 eV, Fig. S17) as usual for this method,[47] the calculated UV absorption spectrum reproduces fairly well the shape (two-band structure) of the experimental one. Moreover, the partial densities of states (PDOS, see Fig. S16) in both the conduction and valence bands are shown to mainly consist of s- and p-valence orbitals, confirming the LC nature of the absorption process in these compounds, showing almost residual contributions of Y(III)-based d orbitals in the frontier MOs.

PL properties of visible emitters ($\mathbf{3_{Eu}}$, $\mathbf{5_{Tb}}$ and $\mathbf{6_{Dy}}$) in the solid state

The photoluminescence properties of the rest of isostructural compounds emitting in the visible range were analysed at room temperature with a similar experimental setup. First, the steady-state spectrum of the powdered sample of $\mathbf{3_{Eu}}$ was recorded. As shown in Fig. 9, the sample emits a bright red colour when excited under UV light of λ_{ex} = 365 nm, confirming good sensitization of this ion by the 2onic ligand.

The RT emission spectrum features the characteristic bands assigned to $^7F_J \leftarrow {}^5D_0$ electronic transitions centred at 592 (for $^7F_1$), 613 (for $^7F_2$), 651 (for $^7F_3$) and 699 nm (for $^7F_4$). There are

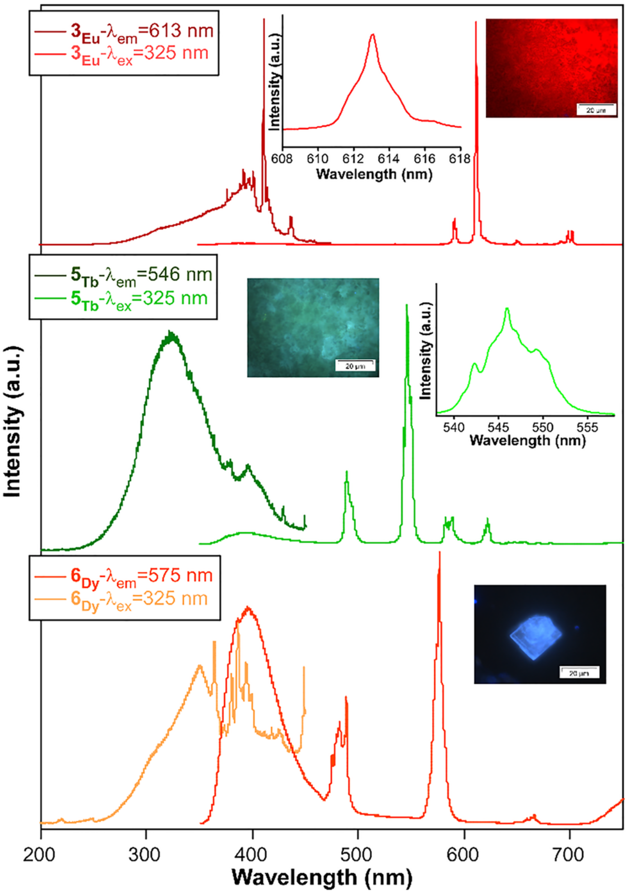

Fig. 9 Excitation and emission spectra of compounds $\mathbf{3_{Eu}}$, $\mathbf{5_{Tb}}$ and $\mathbf{6_{Dy}}$ recorded at RT under an open atmosphere. The inset shows microphotographs of the crystalline samples taken under UV illumination (λ_{ex} = 365 nm).

Table 4 Photophysical properties of compounds $\mathbf{3_{Eu}}$ and $\mathbf{5_{Tb}}$[a]

			τ_{obs}[b] (µs)			
Comp.	λ_{ex}	λ_{em}	293 K-OA	293 K-UV	10 K	QY[c] (%)
$\mathbf{3_{Eu}}$	325	613	368(3)	400(3)	609(3)	12.7
	305	613	354(3)	—	—	9.6
$\mathbf{5_{Tb}}$	325	544	238(5)	117(5)	1130(3)	1.6
	305	544	—	119(5)	—	

[a] Note that excitation wavelengths employed to measure the lifetimes correspond to those fixed by the laser and LED pulsed sources. [b] OA and UV in the columns refer to values recorded in an open atmosphere and under vacuum conditions. [c] Measured only at room temperature due to technical requisites.

two important facts to be noted from these characteristic emissions: (i) the most energetic band intuited at 580 nm, assigned to $^7F_0 \leftarrow {}^5D_0$, presents almost null intensity in contrast to that habitually found for CPs consisting of octa-coordinated Eu(III) ions;[16,31,48–50] (ii) the so-called hypersensitive band (related to the $^7F_2 \leftarrow {}^5D_0$ transition) exhibits an abnormal structureless peak shape (taking into account that the rest of signals are composed of multiplets) with a quite symmetric profile characterized by its narrowness at the top and width at the base, which suggests the presence of less intense unresolved shoulders within this band. The excitation spectrum recorded by fixing the emission at the hypersensitive band shows a broad band peaking at *ca.* 380 nm, assigned to LC excitation, above which many narrow bands, attributed to the intraionic excitations, are distinguished, with that assigned as $^7F_0 \rightarrow {}^5L_6$ dominating the spectrum by far. The much larger intensity of this latter band compared to the LC excitation is clear evidence of the limited antenna effect present in the compound (see further details in Fig. S26). Surprisingly, the decay curve recorded under ligand excitation (at λ_{ex} = 325 nm to avoid the presence of intraionic excitation) for the hypersensitive band presents a monoexponential profile in spite of the presence of two quite distinct independent Eu centres in the crystal structure, with the best fitting giving an emission lifetime of 368(3) µs (Fig. S27). In line with these results, the PLQY for the compound is quite low (Table 4).

A more exhaustive study of the intramolecular energy transfers (IET) was conducted for compound $\mathbf{3_{Eu}}$ according to the equations originally described by Werts *et al.*,[51] which allow estimating that the E_T efficiency from the 2onic ligand to Eu(III) is 73% in the present crystal structure (Table 5, see eqn (S3)–(S5) in the SI for more details).

Moreover, the most representative rates and intensity parameters have been calculated using LUMPAC software based on the experimental spectral data and computational calculations performed on the representative $[Eu(2onic)_4(OH_2)_4]^-$ and $[Eu(\mu\text{-}2onic)_4]^-$ fragments (secondary coordination environment of Eu1 and Eu2 centres, respectively) composing the structure of $\mathbf{3_{Eu}}$ (see the Computational calculations section in the SI for further explanations).[52] The results obtained by this procedure, being practically equal for both models, are close to the experimental ones both regarding the triplet state energies (18780 cm^{-1} from fitting *vs.* the experimental value 19160 cm^{-1}) and the QY values (10.2 *vs.* 12.7%), which supports the calculations although coincidental cancellation of errors cannot be discarded given the large errors associated with the experimental measurement of these parameters (less than 10% of error). The direct-transfer (W) and back-transfer (W_b) rates involved between the ligand and metal were averaged from both fragments taking into account that the two centres are distributed in a 1 : 1 ratio in the structure. As observed in Fig. 10, the largest transfer values involving the triplet mediated state are equally large for both the direct ($T_1 \rightarrow {}^5D_0$) and back-transfer ($^5D_1 \leftarrow T_1$) rates, which supports the fact that although good sensitization of Eu(III) takes place in the compound, the non-radiative component prevails causing poor luminescence efficiency.

Table 5 Radiative and energy transfer parameters calculated for compound $\mathbf{3_{Eu}}$

Media[a]	τ_{rad} (ms)	A_{rad} (s^{-1})	A_{nrad} (s^{-1})	Φ_{Eu}^{Eu}	Φ_{L}^{Eu}	η_{sens}
OA	368(3)	467	2251	0.172	0.127	0.73

[a] These data have been acquired at room temperature for the sample in an open atmosphere.

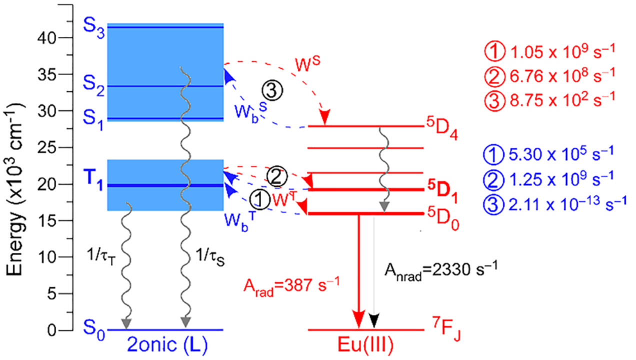

Fig. 10 Energy-level diagram showing the most relevant transfer rates (direct transfer in red and back-transfer in blue) and parameters involved in the photoluminescence performance of compound $\mathbf{3_{Eu}}$. The represented energy levels for the ligand-based singlet and triplets are taken from experimental data, whereas the intraionic states are taken from bibliography.

The coordination of 2onic to the Tb(III) ion in the polymeric structure of compound $\mathbf{5_{Tb}}$ promotes poor pale-green emission as shown in the micrograph taken under UV light. In spite of this, the characteristic four multiplets centred at 493 nm ($^7F_6 \leftarrow {}^5D_4$), 547 nm ($^7F_5 \leftarrow {}^5D_4$), 588 nm ($^7F_4 \leftarrow {}^5D_4$) and 623 nm ($^7F_3 \leftarrow {}^5D_4$) as well as the fifth less intense multiplet around 654 nm ($^7F_J \leftarrow {}^5D_4$, with J = 2, 1 and 0) are well observed using a monochromatic laser beam (λ_{ex} = 325 nm, Fig. 9). Among the bands, the second is the most intense with an intensity that quadruplicates that of the first band, which is in agreement with the results shown by compound $\mathbf{3_{Eu}}$. Under a fixed emission at the most intense band, the excitation spectrum reveals a dominant wide band covering the 250–430 nm range, assigned to the 2onic ligand excitation in agreement with that observed for $\mathbf{4_{Gd}}$, in which some narrow lines attributed to f–f excitations are also distinguished (Fig. S28). The decay curve measured through ligand excitation for $\mathbf{5_{Tb}}$ reveals the occurrence of two well distinguished contributions, which give rise to an average lifetime of 238(5) μs (Fig. S29).

At last, the steady-state emission spectrum of compound $\mathbf{6_{Dy}}$ under UV laser light (λ_{ex} = 325 nm) is composed of both a wide intense band attributed to the ligand's fluorescence and the characteristic narrow bands ascribed to the Dy-centred transitions (Fig. 9). In particular, three single narrow bands are observed at 483, 578 and 667 nm which are assigned to $^6H_J \leftarrow {}^4F_{9/2}$ transitions (where J = 15/2, 13/2 and 11/2), among which the second band dominates the spectrum and the third one is hardly distinguished from the background. This compound presents light blue emission (see single crystal emission in Fig. 9) in agreement with the calculated CIE coordinates (0.246,198). Monitoring the main emission line, the excitation spectrum exhibits a wide band centred at *ca.* 350 nm followed by several narrow bands. The former band, according to that shown for $\mathbf{4_{Gd}}$ and solid state absorption data, corresponds to the ligand-centred excitation whereas the latter bands are attributed to the intraionic f–f transitions. This compound presents very short emission lifetimes (both at the ligand's and Dy-centred characteristic bands) of the order or below the employed lamp's pulse length, so all attempts to estimate the emission lifetimes were unfruitful even if deconvolution strategies were followed.

Overall, the observed luminous performance of these compounds may be explained by Latva's empirical law[53] that rules the efficiency of the antenna effect in Ln-organic compounds on the basis of the energy gap (ΔE) existing between the triplet and Ln-based donor states. In this respect, this ΔE seems to be more appropriate for $\mathbf{3_{Eu}}$ [of 1660 cm^{-1} (ΔT_1(19160 cm^{-1})–$^5D_0$(17500 cm^{-1}))], in contrast to what happens in compounds $\mathbf{5_{Tb}}$ [ΔE being −1640 cm^{-1} (ΔT_1(19160 cm^{-1})–$^5D_4$(20800 cm^{-1}))] and $\mathbf{6_{Dy}}$ [ΔE being −1240 cm^{-1} (ΔT_1(19160 cm^{-1})–$^4F_{9/2}$(20400 cm^{-1}))] in which T$_1$ is below the intraionic emitting excited states of both Tb(III) and Dy(III) ions.[54] Therefore, while high ligand-to-Eu(III) energy transfer seems to take place in $\mathbf{3_{Eu}}$, the corresponding energy transfer is hardly probable in $\mathbf{5_{Tb}}$ and $\mathbf{6_{Dy}}$, in which the back-transfer probability dominates the transfer scenario.

At this point, it is worth highlighting that the compounds described herein perform far below those of related Ln-6m2onic compounds based on the methyl derivative ligand in terms of quantum efficiency (among which Tb-6m2onic presents near unity quantum efficiency, 97%),[31,32] which is quite surprising considering that both compounds consist of essentially the same [Ln(L)$_4$]$^-$ fragment such as that displayed by the Ln2 centre of herein described compounds. This fact seems to be a consequence of the most appropriate electronic structure of 6m2onic to sensitize Ln luminescence, being this in turn a consequence of its higher T$_1$ state energy (of *ca.* 22900 cm^{-1}). However, this disadvantage is more than compensated by the interesting vacuum-/pressure-triggered PL response shown by herein described Ln-2onic compounds (*vide infra* in the "Vacuum-induced modulation of PL properties of visible emitters" section). This behaviour, which as far as we are concerned is a quite unique effect in the field of PL emitters, seems to be derived from their flexible 2D-layered structure that is only available for the 2onic ligand probably due to reduced steric hindrance caused among surrounding ligand copies in the coordination sphere.

PL properties of NIR emitters ($\mathbf{2_{Nd}}$, $\mathbf{7_{Er}}$ and $\mathbf{8_{Yb}}$) in the solid state

To expand the analysis of the PL properties of this family of compounds, we also explored the emission capacity of those Ln compounds potentially emitting in the NIR range in view of the great capacity of the 2onic ligand to sensitize most of Ln ions. It must be emphasized that all measurements were recorded using the He-Cd laser with λ_{ex} = 325 nm as the excitation source and that no traceable emission could be detected for compound $\mathbf{7_{Er}}$ even at temperatures below 30 K. At room temperature, compound $\mathbf{2_{Nd}}$ is the only one showing remarkable NIR emission with a main band sited at *ca.* 1060 nm assigned to the $^4I_{11/2} \leftarrow {}^4F_{3/2}$ transition in addition to a weak band at *ca.* 1320 nm corresponding to the $^4I_{13/2} \leftarrow {}^4F_{3/2}$ transition (Fig. 11a). In contrast, $\mathbf{8_{Yb}}$ shows a frankly weak emission that can solely be intuited in the 980–1040 nm range (Fig. S30), whereas the

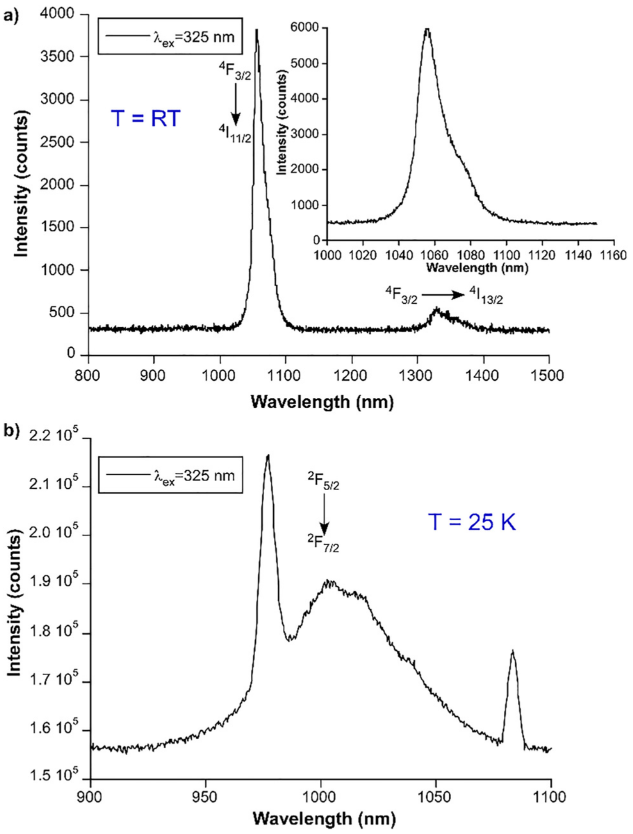

Fig. 11 Emission spectra of NIR emitting compounds in the solid state: (a) room temperature emission of compound $\mathbf{2_{Nd}}$ and (b) emission of compound $\mathbf{8_{Yb}}$ at low temperature.

emission becomes completely evident when the sample is frozen at 25 K (Fig. 11b). As observed at such low temperature, the emission spectrum presents a multiplet composed of a wide band peaking around 1005 nm composed of a main sharp band sited at 977 nm, followed by a wide manifold centred at *ca.* 1009 nm and a separated less intense narrow band at 1084 nm, all of which are characteristic of the intraionic $^2F_{7/2} \leftarrow {}^2F_{5/2}$ transition of the Yb(III) ion as previously shown in the bibliography.[55,56] Lowering the temperature also increases, as expected, the emission capacity of compound $\mathbf{2_{Nd}}$, although the emission bands are unchanged with respect to RT (Fig. S31).

Vacuum-induced modulation of PL properties of visible emitters

In view of the interesting structural dynamic behaviour exhibited by these compounds under vacuum (UV), the photoluminescence properties were analysed under progressive vacuum (reproducing the conditions described in the preceding "Framework response dynamics to temperature and variable pressure" section) to follow the changes occurring in the emission during the reversible vacuum-triggered dehydration/hydration process. The effect of vacuum on the PL properties was carefully analysed on a polycrystalline sample of $\mathbf{3_{Eu}}$ as a representative compound of the isostructural family given its good emission capacity. As observed in Fig. 12, application of vacuum to the sample (denoted as $\mathbf{3_{Eu}}^{\mathbf{UV}}$ hereafter) brought a rapid and significant increase of the emission signal intensity as expected for the absence of molecular oxygen in the cryostat (where a vacuum of *ca.* 10^{-3} mbar was achieved), because those gas molecules are known to greatly quench photoluminescence of solid luminophores.[57,58]

In any case, apart from the previous usual effect, the emission spectrum also displayed some other changes as the vacuum was increased from *ca.* 10^{-5} mbar to the order of 10^{-6} mbar (with the vacuum stabilized for at least ten hours). On the one hand, the hypersensitive band was eventually split into a structured multiplet in which the initial shoulders accompanying the maxima sited at 613 nm are fully resolved (peaking at 611 and 615 nm) and two additional peaks (at 618 and 625 nm) were also shown. On the other hand, the first narrow emission maximum becomes visible at 578 nm for $\mathbf{3_{Eu}}^{\mathbf{UV}}$, which is assigned to the $^7F_0 \leftarrow {}^5D_0$ transition. Both effects are in agreement with symmetry reduction occurring at Eu1 and Eu2 centres present for the DFT-computed partially dehydrated structure based on the theoretical background on Eu(III)-complexes detailed by Binnemans.[59] In this sense, the largely distorted coordination shells present in $\mathbf{3_{Eu}}^{\mathbf{UV}}$ derived from the dehydration, now better described by the C_1 point symbol, cause further splitting of the sublevels of $^{2S+1}L_J$ terms except for J = 0, with the $^7F_2$ term theoretically split into 5 sublevels that match the number of visible signals distinguished in the multiplet of $^7F_2 \leftarrow {}^5D_0$ transition. Moreover, the increase of intensity observed for the electric dipole $^7F_0 \leftarrow {}^5D_0$ transition is justified by the low symmetry Eu(III) sites, known to display intense signals at 580 nm. On their part, the significantly distinct distorted polyhedra of Eu1 and Eu2 sites present in $\mathbf{3_{Eu}}^{\mathbf{UV}}$, pseudo-octahedral in Eu1 and square antiprismatic in Eu2 according to DFT computations (see previous discussion) are well supported in the emission spectrum. In particular, a sextuplet is clearly identified for the magnetic dipole $^7F_1 \leftarrow {}^5D_0$ transition peaking in the 585–600 nm range, concordant with the presence of two independent

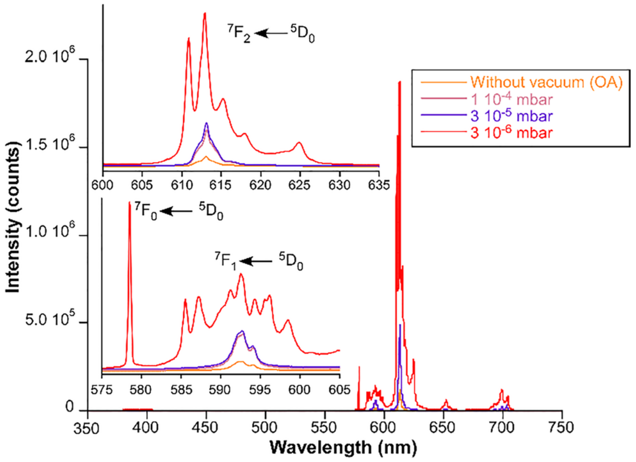

Fig. 12 Fluorescence emission spectra of compound $\mathbf{3_{Eu}}$ at variable vacuum applied to the sample in a closed cryostat under an excitation wavelength of 325 nm. The inset shows the detail of the multiplets assigned to selected transitions. Note that the emission spectrum of $\mathbf{3_{Eu}}^{\mathbf{UV}}$ is shown in red colour (vacuum of 3×10^{-6} bar).

Eu centres in the asymmetric unit, each one giving its own signals taking into account that the $^7F_1$ term cannot further split into more than 3 sublevels. The previous evolution in the emission profile of $\mathbf{3_{Eu}^{UV}}$ is also reflected in the excitation spectrum recorded for λ_{em} = 613 nm (Fig. S32), in which the 2onic-centred band increases its intensity and dominates the spectrum in contrast to its low intensity observed for the neat compound $\mathbf{3_{Eu}}$. To end up with this characterization, it is worth mentioning that the sample immediately recovers its initial emission spectrum once it is left to stand in an open atmosphere for some hours, which confirms the reversibility of the process (Fig. S33). It is also worth noting the fact that vacuum-dependent response is also observed for the rest of isostructural compounds although the effect is not that pronounced (see for instance the subtle changes observed in the excitation spectrum of $\mathbf{5_{Tb}^{UV}}$ and for the rest of counterparts, Fig. S35–S38).

With the aim of further quantifying the spectroscopic changes of pristine (hydrated) and vacuum-triggered (partially dehydrated) compounds, emission lifetimes were measured at the most intense Ln-centred bands. Strikingly, compounds $\mathbf{3_{Eu}^{UV}}$ and $\mathbf{5_{Tb}^{UV}}$ present opposed vacuum-triggered trends, with the lifetime being increased (from 368 to 400 μs) for the Eu-based compound under vacuum in contrast to the drastic decrease (from 238 to 117 μs) for the Tb-based compound (Table 4). The latter evolution is quite surprising because it is in direct contradiction with the expected increase for the removal of O_2 in the system, meaning that additional factors must be affecting the PL of $\mathbf{5_{Tb}^{UV}}$. However, the opposite trend was confirmed to be fully reproducible for both compounds in OA and UV states, allowing the use of lifetime as a characteristic value to identify each compound. Among others, the fact that the vacuum-triggered dehydration mediated structural changes may be shifting the excited triplet state energy is not surprising at all. According to the lifetimes of $\mathbf{3_{Eu}^{UV}}$ and $\mathbf{5_{Tb}^{UV}}$, the T_1 energy should be increasing from its reference value at $\approx$19160 cm^{-1}, which would improve the sensitization of the Eu(III) ion (increasing the T_1–$^5D_0$ gap in $\mathbf{3_{Eu}^{UV}}$) but would worsen the E_T for Tb(III) (decreasing the T_1–$^5D_4$ gap in $\mathbf{3_{Tb}^{UV}}$). Despite the fact that the barycentre of the T_1 state could not be measured for $\mathbf{4_{Gd}^{UV}}$ (because no phosphorescent band is observed under these conditions), data collected for the thermally dehydrated compounds (which promote similar dehydration in the structure, see the next section) point in that sense.

At last, taking advantage of the previous characterization, it could be also confirmed that structural evolution achieved under high pressure of CO_2 gas (see Fig. 6) is reversible and that those metastable configurations identified by PXRD are eventually spontaneously rehydrated back to pristine material when the sample is left exposed to air for one day (Fig. S14), in the same way as observed under vacuum. As detailed in the SI (Fig. S39–S44), the analysis of PL properties for the sample of $\mathbf{3_{Eu}}$ used for CO_2 pressurization experiments reproduces lifetime values of the pristine compound at RT and OA, and it also shows reproducible changes in both the PL spectra and lifetime values during a whole vacuum-assisted dehydration/rehydration cycle.

In the same line, X-ray photoelectron spectroscopy (XPS) measurements conducted on both the fresh sample of $\mathbf{3_{Eu}}$ and the rehydrated sample of $\mathbf{3_{Eu}}$ recovered from gas-pressurization experiments show coincident results on the analytical content (Table S6), thus further confirming the spontaneous reversibility of the pressurization-triggered dehydration by simply exposing the sample to OA conditions (see the S14 section in the SI for detailed explanation).

Therefore, these materials exhibit reproducible and reversible vacuum-triggered luminescence response that renders them promising candidates for luminescence sensors capable of monitoring variations in pressure and humidity.

Modulation of PL properties through temperature-assisted dehydration

Considering both the limited applicability of the thermal dehydration of these compounds, which become amorphous during the initial dehydration stage, and the impossibility to recycle the fully dehydrated products (heated at 215 °C for 3 h and hereafter denoted as $\mathbf{3_{Eu}^{D}}$ and $\mathbf{5_{Tb}^{D}}$) into pristine compounds, the characterization of these materials during their thermal treatment has been summarized here. A first inspection of the PL spectra of $\mathbf{3_{Eu}^{D}}$ (Fig. S45) reveals two important changes with respect to the original compound. On the one hand, the first band peaking at 578 nm (assigned to the $^7F_0 \leftarrow {}^5D_0$ transition) is again visible in the emission spectrum, and on the other hand, a wide band with the maximum centred at *ca.* 350 nm is observed to dominate the excitation spectrum. These changes reinforce the idea that both vacuum and thermal treatments promoting dehydration of the samples exert a similar effect in the PL response of the material. A distinctive feature for these spectra with respect to those of their pristine parent compounds $\mathbf{3_{Eu}}$ and $\mathbf{5_{Tb}}$ is the lack of fine structure in the characteristic Ln-centred bands, which is attributed to the loss of crystallinity. The emission lifetimes estimated by the exponential fitting of the decay curves for the dehydrated compounds $\mathbf{3_{Eu}^{D}}$ and $\mathbf{5_{Tb}^{D}}$ reveal slightly shorter values compared to the original compounds (Table 6, see also Fig. S46 and S48), which contrasts with the overall improvement

Table 6 Lifetime results for the Eu- and Tb-based compounds measured under variable conditions

				τ_{obs} (μs)		
Comp.[a]	Med.[b]	λ_{ex}	λ_{em}	293 K	10 K	QY (%)
Eu-based compound						
As-synt.	OA ($\mathbf{3_{Eu}}$)	325	613	368(3)	609(3)	12.7
	UV ($\mathbf{3_{Eu}^{UV}}$)	325	613	400(3)		—
Dehyd.	OA ($\mathbf{3_{Eu}^{D}}$)	340	614	328(4)	771(5)	16.5
	UV ($\mathbf{3_{Eu}^{D\text{-}V}}$)	340	614	303(4)		—
Tb-based compound						
As-synt.	OA ($\mathbf{5_{Tb}}$)	325	544	238(5)	1130(3)	1.6
	UV ($\mathbf{5_{Tb}^{UV}}$)	305	544	117(5)		—
Dehyd.	OA ($\mathbf{5_{Tb}^{D}}$)	340	544	180(2)	774(5)	13.4
	UV ($\mathbf{5_{Tb}^{D\text{-}V}}$)	340	544	152(2)		—

[a] Refers to the as-synthesized or the thermally dehydrated compound. [b] OA and UV have their previously mentioned meanings: open atmosphere and under vacuum, respectively.

of their emission efficiency. Such an increase in QY, particularly remarkable for the Tb-based compound, seems to be mainly derived from a drastic decrease of the non-radiative rate, especially when considering that the energy shift occurring for the T_1 state in the dehydrated compounds (T_1 lies at *ca.* 20000 cm^{-1} in $\mathbf{4_{Gd}}^{\mathbf{D}}$, see Fig. S52) might result, *a priori*, in less efficient E_T for $\mathbf{5_{Tb}}^{\mathbf{D}}$ (ΔE becomes optimal for $\mathbf{3_{Eu}}^{\mathbf{D}}$, being now of 2500 cm^{-1}, but unfavourable for $\mathbf{5_{Tb}}^{\mathbf{D}}$ −800 cm^{-1}). The mentioned enhancement for $\mathbf{5_{Tb}}^{\mathbf{D}}$ is also accompanied by the relative increase of the characteristic intra-Tb bands with respect to the LC band as confirmed by the colour change (from light blue in $\mathbf{5_{Tb}}$ to light green in $\mathbf{5_{Tb}}^{\mathbf{D}}$) observed in micro-PL images taken under λ_{ex} = 365 nm (Fig. S54).

On another level, when the samples are placed under high vacuum (hereafter $\mathbf{3_{Eu}}^{\mathbf{D\text{-}V}}$ and $\mathbf{5_{Tb}}^{\mathbf{D\text{-}V}}$) they do not show such drastic changes as those discussed for pristine compounds, probably because $\mathbf{3_{Eu}}^{\mathbf{D}}$ and $\mathbf{5_{Tb}}^{\mathbf{D}}$ are already fully dehydrated, which reasonably prevents the structural changes derived from vacuum-triggered partial dehydration. Moreover, the emission lifetimes are slightly decreased for both solids by the effect of vacuum (see Fig. S46 and S48 and data in Table 6).

The effect of lowering temperature was also studied for these samples in view of their rich PL response to physical factors, seeking for potential thermometric activity. At this point, it must be noticed that the procedure employed to cool samples down to cryogenic temperature requires previous application of vacuum on them and thus, all previous effects will be omitted here. Starting from pristine materials, the excitation and emission spectra of $\mathbf{3_{Eu}}^{\mathbf{UV}}$ at 12 K reflect sizeable increases in both the intensity of the emission bands (particularly for the hypersensitive one) and the observed lifetime (Fig. S56, see also Table 6), as expected for the rigidity gained by the molecules in such a frozen state. On its part, the low-temperature response for compound $\mathbf{5_{Tb}}^{\mathbf{UV}}$ is comparatively more pronounced in both the shape of PL bands (Fig. S57 and S58) and the emission lifetime (shown to increase by more than 965% of its value at RT (from 117 to 1130 μs, Table 5). In spite of these latter changes, both compounds exhibited poor linear dependence with temperature (Fig. S60a) that translated into low thermometric activity, which can be summarized by a maximum relative sensitivity (S_m) of 0.54% K^{-1} at a temperature of 30 K for $\mathbf{3_{Eu}}^{\mathbf{UV}}$ and of 0.70% K^{-1} at 110 K for $\mathbf{5_{Tb}}^{\mathbf{UV}}$, thus far from those best performing Ln-based reported thermometers.[25] An even poorer performance was also found for the dehydrated compounds $\mathbf{3_{Eu}}^{\mathbf{D\text{-}V}}$ and $\mathbf{5_{Tb}}^{\mathbf{D\text{-}V}}$ (S_m = 0.09% K^{-1} at 135 K and 0.12% K^{-1} at 45 K, respectively, Fig. S61 and S62). At last, the measurements were also repeated for the *in situ* thermally dehydrated compound $\mathbf{5_{Tb}}$ (eventually rendering $\mathbf{5_{Tb}}^{\mathbf{D}}$, Fig. S60b). Nonetheless, the poor performance shown by this compound (S_m of 0.75% K^{-1} at 513 K), in addition to the irreversibility of the dehydration process which causes sample amorphization, suggest that the dehydrated compounds could only be single-use thermometers, far from ideal thermometers.

PL properties of the water-dissolved complexes

These compounds present quite good solubility in water given their ionic crystal structure (composed of a cationic framework containing perchlorate anions), so their PL emissive capacity was also studied in aqueous solutions. In order to ensure good comparability for all compounds, solutions of compounds $\mathbf{3_{Eu}}$, $\mathbf{5_{Tb}}$ and $\mathbf{6_{Dy}}$ were prepared by dissolving 5 mg of each polycrystalline sample in 4 mL of water (*i.e.* 1.25 mg mL^{-1}, hereafter $\mathbf{3_{Eu}@H_2O}$, $\mathbf{5_{Tb}@H_2O}$ and $\mathbf{6_{Dy}@H_2O}$). As observed in the photographs taken for these samples (Fig. S73), the solutions acquire characteristic colours upon irradiation with UV light, a fact that seems to indicate that the Ln-based chromophores present in the crystalline solid are being preserved in the solution, a fact that is in agreement with the good emission capacity displayed by the 2onic ligand itself (Fig. S74 and S75). The UV-Vis spectra recorded on these solutions resemble the patterns of diffuse reflectance measurements, which confirms the integrity of the complexes in solution (Fig. S76). In any case, ^{1}H nuclear magnetic resonance (NMR) spectra were acquired for both the compound $\mathbf{1_Y@H_2O}$ (given its diamagnetic nature) and an equivalent aqueous solution of the free 2onic ligand. The comparison of these patterns confirms that $\mathbf{1_Y@H_2O}$ contains no free ligand and that the dissolved species are coordinated in agreement with the lower chemical shift observed (Fig. S70). Moreover, the dissolved complex is shown to remain stable in solution as proved by the reproducibility of the NMR pattern collected for the aqueous solution of $\mathbf{1_Y@H_2O}$ during several weeks after its preparation (see Fig. S71). The hypothesis that $[\mathrm{Ln(2onic)_4}]^-$ are the dominating stable species of the aqueous solution is confirmed by ESI-MS (electrospray ionization-mass spectrometry), because the analysis performed on a $\mathbf{1_Y@H_2O}$ aliquot reveals a dominating signal centred at an *m*/*z* of 641 with a periodicity of one unit (Fig. S72). Overall, the dissolved complexes present very good emission properties as corroborated by the PL spectra, which show patterns resembling the solid-state spectra. On the one hand, the excitation spectra exhibit a dominating band (covering the 230–350 nm range) in which two marked maxima are clearly distinguished at *ca.* 305 and 330 nm regions corresponding to the previously mentioned ligand-centred S_1 and S_2 excited states, respectively, in agreement with the UV-Vis spectra recorded for the solutions (Fig. S77–S79). The fact that intraionic f–f absorptions are hardly observed suggests that the antenna effect is still large in the complexes even when they are surrounded by water molecules, even brighter than in the solid state as reflected by the absolute QYs measured for the solutions using distilled water as blank (Table 5). The emission spectra keep the excitation-dependent effect already studied at the solid state, with the ligand-centred emission band displaying higher intensity through the S_1 state excitation ($\lambda_{ex} \approx$ 330 nm) than through the S_2 state excitation ($\lambda_{ex} \approx$ 305 nm), whereas the characteristic Ln-centred emissions, lacking the fine structure observed for the solid state, remain almost independent of the excitation energy. In fact, the lifetimes measured for the main emission lines of the compounds confirm the latter by showing almost identical values (Fig. S80–S82 and Table 7). In this regard, it is especially worth noting the case of the Dy-based compound, since emission lifetimes are significantly increased for the dissolved complex ($\tau \approx$ 5 μs) with respect to the solid state, where the lifetimes

Table 7 Lifetime results for the as-synthesized and dehydrated compounds under variable media

Comp.[a]	Med.[b]	λ_{ex}	λ_{em}	τ_{obs} (μs)	QY (%)
Eu-based compound					
$\mathbf{3_{Eu}}$	OA (solid state)	325	613	368(3)	12.7
	Aqueous ($\mathbf{3_{Eu}@H_2O}$)	335	612	193(2)	18.5
Dehydr.	OA ($\mathbf{3_{Eu}}^{\mathbf{D}}$)	340	614	328(4)	16.5
	Aqueous ($\mathbf{3_{Eu}}^{\mathbf{D}}\mathbf{@H_2O}$)	330	612	178(2)	17.7
Tb-based compound					
$\mathbf{5_{Tb}}$	OA (solid state)	325	544	238(5)	1.6
	Aqueous ($\mathbf{5_{Tb}@H_2O}$)	330	544	484(5)	21.5
Dehydr.	OA ($\mathbf{5_{Tb}}^{\mathbf{D}}$)	340	544	180(2)	13.4
	Aqueous ($\mathbf{5_{Tb}}^{\mathbf{D}}\mathbf{@H_2O}$)	304	544	407(3)	14.7
Dy-based compound					
$\mathbf{6_{Dy}}$	OA (solid state)	—	—	—	<1
	Aqueous ($\mathbf{6_{Dy}@H_2O}$)	305	575	5.13(1)	3.5
Dehydr.	OA ($\mathbf{6_{Dy}}^{\mathbf{D}}$)	—	—	—	<1
	Aqueous ($\mathbf{6_{Dy}}^{\mathbf{D}}\mathbf{@H_2O}$)	305	575	5.01(1)	3.0

[a] It refers to the as-synthesized or the thermally dehydrated compound. [b] OA refers to an open atmosphere for the solid state conditions.

were shorter than 1 ns (below the detection limit of the pulsed source). A comparative analysis of $\mathbf{3_{Eu}@H_2O}$ and $\mathbf{3_{Eu}@D_2O}$ solutions further confirms the lack of coordinated water molecules of the dissolved complex in aqueous solution ($q = 0.0049$, where q stands for the number of coordination H_2O molecules, see eqn (S2) and Fig. S83 and S84 in the SI).[60]

With respect to the dehydrated samples, they are also quite soluble in water, which allows one to prepare solutions of the same concentration (1.25 mg mL^{-1}, referred to as $\mathbf{3_{Eu}}^{\mathbf{D}}\mathbf{@H_2O}$, $\mathbf{5_{Tb}}^{\mathbf{D}}\mathbf{@H_2O}$ and $\mathbf{6_{Dy}}^{\mathbf{D}}\mathbf{@H_2O}$) to perform comparative measurements (Fig. S85–S91). *A priori*, although the excitation wavelength-dependence behaviour is reproduced for these samples, their PL signal is slightly weaker than for the corresponding solutions based on as-synthesized compounds as confirmed by the shorter lifetimes and lower QYs registered.

On another level, aqueous solutions of 1.25 mg mL^{-1} were also prepared for NIR emitters to check if this particular luminescence is also preserved in water. Despite the fact that the signal intensity is strongly decreased, $\mathbf{2_{Nd}@H_2O}$ and $\mathbf{8_{Yb}@H_2O}$ solutions keep their characteristic emission although the water medium (Fig. S92 and S93) is considered as an excellent quencher of Lns' PL emission.[60,61] As far as we are concerned, the occurrence of PL emission in the NIR by water-dissolved Ln complexes is not common and the number of stable compounds displaying strong emission is quite scarce and limited to the use of macrocyclic ligands able to establish multiple chelating rings with Lns.[62,63] Therefore, the present compounds consisting of small 2onic ligands may be taken as inspiring results to develop competitive NIR-emitting compounds in future.

Conclusions

A family of eight Ln-based CPs featuring a cationic 2D framework tailored by the 2onic ligand that contains lattice perchlorate anions and water molecules is described and physico-chemically characterized in detail. The framework, consisting of two distinct distorted Ln centres close to a triangular dodecahedron and square antiprism, is quite flexible and prone to undergo structural dynamics under the application of heat or vacuum/pressure to the sample. While irreversible uncontrolled dehydration by heating the samples within the 110–210 °C temperature range leads to amorphous products, the crystal structure experiences reversible partial dehydration (with the loss of two lattice and two coordination water molecules) under both high vacuum and gas pressurization. PDFT optimizations of the structure of $\mathbf{1_Y}$ allow visualizing the structural changes occurring under vacuum and particularly the increased distortion of the coordination polyhedra in the partially dehydrated compound. Collectively, the gas-pressure experiments demonstrate vacuum-triggered, air-locked restructuring and CO_2-driven convergence, revealing a controllable, path-dependent relaxation of the framework.

In parallel, a detailed experimental and calculated photophysical study has been accomplished to fully understand the luminescence mechanism. On the one hand, absorption spectra are well reproduced by complementary DOS on the PDFT-optimized structure of $\mathbf{1_Y}$ and TDDFT on an isolated optimized model of $\mathbf{4_{Gd}}$, permitting to understand key electronic transitions governing the excitation. On the other hand, semi-empirical methods on suitable models of $\mathbf{3_{Eu}}$ clarify the main ETs in the compound and confirm that the 2onic ligand sensitizes Eu(III) emission (which displays a modest QY of *ca.* 13%) whereas it provides poor Tb(III)-based emission (QY less than 2%), which also concords with Latva's law on the basis of the energy gap between the ligand-centred triplet state and the Ln-centred intraionic excited states. While thermal treatment of these materials presents serious limitations due to uncontrolled and irreversible dehydration rendering amorphous compounds, in spite of the interesting behaviour found in their thermometric PL, vacuum-assisted and gas pressurization mediated dehydration trigger reversible PL-response of compounds $\mathbf{3_{Eu}}$ and $\mathbf{5_{Tb}}$. Among all changes induced by changes in the ETs governing PL properties, changes in their emission lifetimes, showing opposed trends (increase for $\mathbf{3_{Eu}}$ and steep decrease for $\mathbf{5_{Tb}}$), can be taken as main reference values of the process. In fact, being consistently reproduced along various dehydration/rehydration cycles, lifetimes allow identifying hydration stages of the compounds, supporting their use as pressure and humidity sensors.

Taking advantage of the solubility of these compounds in water, PL properties of water-dissolved complexes have been studied. As confirmed by ESI-MS, the crystal structure appears to be split into discrete complexes that remain stable in solution without apparent speciation (*i.e.* excision to free ligand) for at least one month as confirmed by ^{1}H NMR analysis. Surprisingly, the aqueous solutions of these complexes exhibit even higher emission efficiency than solid samples, with the Eu(III)-based complex leading the group with a QY of 18.5%. At last, it must be also emphasized that Nd- and Yb-based compounds also retain characteristic NIR emissions in aqueous solution.

Overall, the interesting vacuum-/pressure-induced PL response and emission capacity of the water-soluble complexes underline their potential use as physical sensors or luminescence probes in biological media.

Experimental section

Chemicals

All chemicals were of reagent grade and were used as commercially obtained without any further purification.

Synthesis of $\{[M_2(\mu_3\text{-2onic})_4(H_2O)_4](ClO_4)_2\cdot 2H_2O\}_n$ [where M(III) = Y (1_Y), Nd(2_{Nd}), Eu (3_{Eu}), Gd (4_{Gd}), Tb (5_{Tb}), Dy (6_{Dy}), Er (7_{Er}) and Yb (8_{Yb})]

All compounds were obtained by mixing the corresponding rare-earth(III) chloride hydrated salt (0.20 mmol, using 0.0607 g for $YCl_3\cdot 6H_2O$, 0.0717 g for $NdCl_3\cdot 6H_2O$, 0.0733 g for $EuCl_3\cdot 6H_2O$, 0.0743 g for $GdCl_3\cdot 6H_2O$, 0.0756 g for $TbCl_3\cdot 6H_2O$, 0.0754 g for $DyCl_3\cdot 6H_2O$, 0.0763 g for $ErCl_3\cdot 6H_2O$ and 0.0775 g for $YbCl_3\cdot 6H_2O$), H2onic (0.40 mmol, 0.0556 g), $NaClO_4\cdot H_2O$ (0.80 mmol, 0.1124 g) and CH_3COONa (0.40 mmol, 0.0328 g) in 10 mL of distilled water, followed by stirring at RT until their complete dissolution. The aqueous solutions were placed in Teflon-lined closed vessels to be heated under hydrothermal conditions for 3 days at 120 °C and then slowly cooled down to room temperature through a one-day ramp. Then, the solutions were left at room temperature in open glass vials for 2–3 days, after which light-colourless square-shaped single crystals were grown. The crystals were filtered and washed with water and methanol several times. The yield was 60–70% based on the metal.

Chemical characterization

Elemental analyses, FTIR spectral analysis and thermal analyses were performed on powdered samples of the compounds as detailed in the SI (see the S1 section). Moreover, absorption spectra were measured using a UV-2600 UV-Vis Shimadzu spectrophotometer. X-ray photoelectron spectroscopy (XPS) measurements were performed on a Versaprobe III Physical Electronics (ULVAC) system (see the SI for more information).

X-ray diffraction data collection and structure determination

The single crystal X-ray diffraction (SCXD) data used for structure determination were recorded at 100(2) K on suitable single crystals of compounds $\mathbf{3_{Eu}}$, $\mathbf{4_{Gd}}$ and $\mathbf{5_{Tb}}$ on a Bruker VENTURE diffractometer (see further details in the SI). The structure was refined with the SHELXL program[64] including all reflections and full-matrix least-squares on F^2 employing the Olex2 software.[65] All details about the refinement of the structures can be found in Table S1 of the SI. The cif file can be found in the Cambridge Crystallographic Data Center as supplementary publication with no. CCDC 2456148–2456153.

The powder X-ray diffraction (PXRD) patterns collected on polycrystalline samples to confirm their purity were acquired on a Philips X'PERT powder diffractometer as detailed in the SI.

On another level, variable-pressure PXRD experiments under argon and synthetic air as well as additional experiments of the samples under CO_2 pressure were performed on a BRUKER D8 Advance A25 diffractometer as detailed in the SI (see the S1 section).

Photoluminescence measurements

Photoluminescence measurements were recorded at variable temperature and pressure in a closed-cycle helium cryostat enclosed in an Edinburgh Instruments FLS980 spectrometer using several excitation sources as detailed in the SI. Microluminescence photographs were taken using an Olympus optical microscope equipped with a Hg lamp. Quantum yield measurements were performed using a properly calibrated Horiba Quanta-φ integrating sphere coupled to an Oriel Instruments MS257 lamp and an iHR550 spectrometer from Horiba.

Computational details

The Gaussian 16 package[66] was employed for optimizing the geometries of a suitable model of compound $\mathbf{4_{Gd}}$, using the B3LYP level of theory with the def2-TZVP basis set[67] for all atoms and the corresponding relativistic pseudo-potential for Gd(III). The calculations of the UV-Vis spectra were carried out with ORCA software[68] using the same model chemistry and including Grimme's empirical dispersion correction,[69] running first a CASSCF calculation with CAS(3,3) to properly describe the excitation scenario of optimized models, and MC-RPA calculations on top of the latter for an accurate description of the multiconfigurational states. With regard to the calculations about the E_T rates with LUMPAC software,[52] both $[Eu(\mu\text{-2onic})_4]^-$ and $[Eu(2onic)_4(OH_2)_4]^-$ fragments were first optimized with the Sparkle/RM1 model and the charge factors (g) and polarizabilities (α) of the donor set atoms estimated (Table S6). In view of the similar results for these two models, herein presented values correspond to averaged results. At last, periodic density-functional theory (DFT) calculations were performed using the code CASTEP.[36] The calculations employed the GGA-PBE exchange–correlation functional[70] together with ultrasoft pseudopotentials, a plane-wave cutoff of 490 eV and a Monkhorst–Pack grid of 1 × 1 × 2 for the k-point sampling. To account for the non-covalent interactions the TS dispersion correction scheme[71] was used. To compute density of state plots and bandgap values, energy calculations were performed on models derived from the periodic DFT geometry optimization performed upon the crystal structure of compound $\mathbf{1_Y}$.

Conflicts of interest

There are no conflicts to declare.

Data availability

The data supporting this article have been included as part of the supplementary information (SI) and will be available from authors upon reasonable request. Supplementary information is available. See DOI: **https://doi.org/10.1039/d6qm00036c**.

CCDC 2456148–2456153 ($\mathbf{1_Y}$, $\mathbf{2_{Nd}}$, $\mathbf{3_{Eu}}$, $\mathbf{4_{Gd}}$, $\mathbf{5_{Tb}}$ and $\mathbf{6_{Dy}}$) contain the supplementary crystallographic data for this paper.[72a–f]

Acknowledgements

This work has been funded by Red Guipuzcoana de Ciencia, Tecnología e Innovación (FA-EP-2025-0408; DG25/10), Gobierno Vasco/Eusko Jaurlaritza, for both the funding for consolidated group (IT1755-22 and IT1500-22) as well as the ELKARTEK 2025 research program (ELKARTEK25/21, KK-2025/00022), the Spanish Ministry of Science, Innovation and Universities (PID2022-138968NB-C22 project funded by MCIU/AEI/10.13039/501100011033 and by ERDF EU) and Junta de Andalucía (FQM-394 and P21_00386). LRB thanks UPV/EHU for his predoctoral fellowship. The authors acknowledge the technical and human support provided by SGIker (UPV/EHU/ERDF, EU).

Notes and references

1 K. Binnemans, Lanthanide-Based Luminescent Hybrid Materials, *Chem. Rev.*, 2009, **109**, 4283–4374.

2 J. C. G. Bünzli, *Handbook on the Physics and Chemistry of Rare Earths*, Elsevier, Amsterdam, 2016.

3 J. C. G. Bünzli and S. V. Eliseeva, Intriguing Aspects of Lanthanide Luminescence, *Chem. Sci.*, 2013, **4**, 1939–1949.

4 S. V. Eliseeva, J.-C. G. Bünzli, D. R. Dreyer, S. Park, C. W. Bielawski and R. S. Ruoff, Lanthanide Luminescence for Functional Materials and Bio-Sciences, *Chem. Soc. Rev.*, 2009, **39**, 189–227.

5 T. Xian, Q. Meng, F. Gao, M. Hu and X. Wang, Functionalization of Luminescent Lanthanide Complexes for Biomedical Applications, *Coord. Chem. Rev.*, 2023, **474**, 214866.

6 J. Cepeda, A. Rodríguez-Diéguez and A. Salinas-Castillo, in *Metal-Organic Frameworks in Biomedical and Environmental Field*, ed. P. Horcajada and S. Rojas, Springer, Cham, 2021.

7 S. Faulkner, S. J. A. Pope and B. P. Burton-Pye, Lanthanide Complexes for Luminescence Imaging Applications, *Appl. Spectrosc. Rev.*, 2005, **40**, 1–31.

8 N. H. Ly and S.-W. Joo, Recent Advances in Cancer Bioimaging Using a Rationally Designed Raman Reporter in Combination with Plasmonic Gold, *J. Mater. Chem. B*, 2020, **8**, 186–198.

9 A. Abdollahi, H. Roghani-Mamaqani, B. Razavi and M. Salami-Kalajahi, Photoluminescent and Chromic Nanomaterials for Anticounterfeiting Technologies: Recent Advances and Future Challenges, *ACS Nano*, 2020, **14**, 14417–14492.

10 H. Zhou, J. Han, J. Cuan and Y. Zhou, Responsive Luminescent MOF Materials for Advanced Anticounterfeiting, *Chem. Eng. J.*, 2022, **431**, 134170.

11 M. Maxeiner, R. Maile, M. Cuvalli, A. Wolf, A. Komal, R. Oestreich, C. Janiak, K. Mandel, A. Knebel and K. Müller-Buschbaum, NanoMOF-Based Multilevel Anti-Counterfeiting by a Combination of Visible and Invisible Photoluminescence and Conductivity, *Adv. Funct. Mater.*, 2025, 2500794.

12 X. Chen, T. Sun and F. Wang, Lanthanide-Based Luminescent Materials for Waveguide and Lasing, *Chem. – Asian J.*, 2020, **15**, 21–33.

13 M. Tu, H. Reinsch, S. Rodríguez-Hermida, R. Verbeke, T. Stassin, W. Egger, M. Dickmann, B. Dieu, J. Hofkens, I. F. J. Vankelecom, N. Stock and R. Ameloot, Reversible Optical Writing and Data Storage in an Anthracene-Loaded Metal–Organic Framework, *Angew. Chem., Int. Ed.*, 2019, **58**, 2423–2427.

14 S. Dang, J. H. Zhang and Z. M. Sun, Tunable Emission Based on Lanthanide(III) Metal–Organic Frameworks: An Alternative Approach to White Light, *J. Mater. Chem.*, 2012, **22**, 8868–8873.

15 P. P. Ferreira da Rosa, Y. Kitagawa and Y. Hasegawa, Luminescent Lanthanide Complex with Seven-Coordination Geometry, *Coord. Chem. Rev.*, 2020, **406**, 213153.

16 À. Tubau, L. Rodríguez, P. Pander, L. Weatherill, F. B. Dias, M. Font-Bardía and R. Vicente, Slow Magnetic Relaxation and Luminescence Properties in β-Diketonate Lanthanide(III) Complexes. Preparation of Eu(III) and Yb(III) OLED Devices, *J. Mater. Chem. C*, 2024, **12**, 8127–8144.

17 K. Nehra, A. Dalal, A. Hooda, S. Bhagwan, R. K. Saini, B. Mari, S. Kumar and D. Singh, Lanthanides β-Diketonate Complexes as Energy-Efficient Emissive Materials: A Review, *J. Mol. Struct.*, 2022, **1249**, 131531.

18 G. F. De Sá, O. L. Malta, C. De Mello Donegá, A. M. Simas, R. L. Longo, P. A. Santa-Cruz and E. F. Da Silva, Spectroscopic properties and design of highly luminescent lanthanide coordination complexes, *Coord. Chem. Rev.*, 2000, **196**, 165–195.

19 C. Alexander, Z. Guo, P. B. Glover, S. Faulkner and Z. Pikramenou, Luminescent Lanthanides in Biorelated Applications: From Molecules to Nanoparticles and Diagnostic Probes to Therapeutics, *Chem. Rev.*, 2025, **125**, 2269–2370.

20 A. Dalal, K. Nehra, A. Hooda, D. Singh, P. Kumar, S. Kumar, R. S. Malik and B. Rathi, Luminous lanthanide diketonates: Review on synthesis and optoelectronic characterizations, *Inorg. Chim. Acta*, 2023, **550**, 121406.

21 B. Li, H. M. Wen, Y. Cui, G. Qian and B. Chen, Multifunctional Lanthanide Coordination Polymers, *Prog. Polym. Sci.*, 2015, **48**, 40–84.

22 D. Parker, J. D. Fradgley and K. L. Wong, The Design of Responsive Luminescent Lanthanide Probes and Sensors, *Chem. Soc. Rev.*, 2021, **50**, 8193–8213.

23 P. Kumar, S. Singh and B. K. Gupta, Future prospects of luminescent nanomaterial based security inks: from synthesis to anti-counterfeiting applications, *Nanoscale*, 2016, **8**, 14297–14340.

24 Y. Zhao, H. Zeng, X. W. Zhu, W. Lu and D. Li, Metal–Organic Frameworks as Photoluminescent Biosensing Platforms: Mechanisms and Applications, *Chem. Soc. Rev.*, 2021, **50**, 4484–4513.

25 J. Rocha, C. D. S. Brites and L. D. Carlos, Lanthanide Organic Framework Luminescent Thermometers, *Chem. – Eur. J.*, 2016, **22**, 14782–14795.

26 A. Das, S. Bej, N. R. Pandit, P. Banerjee and B. Biswas, Recent Advancements of Metal–Organic Frameworks in Sensing Platforms: Relevance in the Welfare of the Environment and the Medical Sciences with Regard to Cancer and SARS-CoV-2, *J. Mater. Chem. A*, 2023, **11**, 6090–6128.

27 D. Banerjee, Z. Hu and J. Li, Luminescent Metal–Organic Frameworks as Explosive Sensors, *Dalton Trans.*, 2014, **43**, 10668–10685.

28 O. Pajuelo-Corral, I. Ortiz-Gómez, J. A. García, A. Rodríguez-Diéguez, I. J. Vitórica-Yrezábal, A. Salinas-Castillo, J. M. Seco and J. Cepeda, A Family of Cd(II) Coordination Polymers Constructed from 6-Aminopicolinate and Bipyridyl Co-Linkers: Study of Their Growth in Paper and Photoluminescence Sensing of Fe^{3+} and Zn^{2+} Ions, *Dalton Trans.*, 2024, **53**, 12138–12151.

29 J. R. Askim, M. Mahmoudi and K. S. Suslick, Optical Sensor Arrays for Chemical Sensing: The Optoelectronic Nose, *Chem. Soc. Rev.*, 2013, **42**, 8649–8682.

30 Y. Hasegawa and Y. Kitagawa, Luminescent Lanthanide Coordination Polymers with Transformative Energy Transfer Processes for Physical and Chemical Sensing Applications, *J. Photochem. Photobiol., C*, 2022, **51**, 100485.

31 L. Razquin-Bobillo, A. Zabala-Lekuona, J. A. García, A. Rodríguez-Diéguez and J. Cepeda, Water Soluble Rare-Earth(III) Based Coordination Polymers with Luminescence Versatility in Various Media: Reaching the Sky of Quantum Efficiency, *Adv. Opt. Mater.*, 2024, **12**, 2401472.

32 L. Razquin-Bobillo, J. A. García, R. Hernández, A. Rodríguez-Diéguez and J. Cepeda, A family of luminescent heterometallic coordination polymers based on lanthanide(III) ions and 6-methyl-2-oxonicotinate: near-infrared/visible emitters and colour fine-tuning, *CrystEngComm*, 2024, **26**, 6707–6718.

33 N. Xu, W. Shi, D. Z. Liao, S. P. Yan and P. Cheng, Template Synthesis of Lanthanide (Pr, Nd, Gd) Coordination Polymers with 2-Hydroxynicotinic Acid Exhibiting Ferro-/Antiferromagnetic Interaction, *Inorg. Chem.*, 2008, **47**, 8748–8756.

34 N. Xu, C. Wang, W. Shi, S. P. Yan, P. Cheng and D. Z. Liao, Magnetic and Luminescent Properties of Sm, Eu, Tb, and Dy Coordination Polymers with 2-Hydroxynicotinic Acid, *Eur. J. Inorg. Chem.*, 2011, 2387–2393.

35 L. Razquin-Bobillo, O. Pajuelo-Corral, A. Zabala-Lekuona, A. Rodríguez-Diéguez and J. Cepeda, An Experimental and Theoretical Study of the Magnetic Relaxation in Heterometallic Coordination Polymers Based on 6-Methyl-2-Oxonicotinate and Lanthanide(III) Ions with Square Antriprismatic Environment, *Dalton Trans.*, 2022, **51**, 16243–16255.

36 S. J. Clark, M. D. Segall, C. J. Pickard, P. J. Hasnip, M. I. J. Probert, K. Refson and M. C. Payne, First principles methods using CASTEP, *Z. Kristallogr.*, 2005, **220**, 567–570.

37 S. Horike, S. Shimomura and S. Kitagawa, Soft porous crystals, *Nat. Chem.*, 2009, **1**, 695–704.

38 N. Monni, S. Dey, V. Garcia-Lopez, M. Oggianu, J. J. Baldovi, M. L. Mercuri, M. Clemente-Leon and E. Coronado, Tunable SIM properties in a family of 3D anilato-based lanthanide-MOFs, *Inorg. Chem. Front.*, 2024, **11**, 5913–5923.

39 L. Vanduyfhuys, S. M. J. Rogge, J. Wieme, S. Vandenbrande, G. Maurin, M. Waroquier and V. Van Speybroeck, Thermodynamic insight into stimuli-responsive behaviour of soft porous crystals, *Nat. Commun.*, 2018, **9**, 204.

40 A. V. Neimark, F. X. Coudert, C. Triguero, A. Boutin, A. H. Fuchs, I. Beurroies and R. Denoyel, Structural Transitions in MIL-53 (Cr): View from Outside and Inside, *Langmuir*, 2011, **27**, 4734–4741.

41 M. Arjmandi, E. Aytaç, M. Khayet and N. Hilal, Next-generation MOFs for atmospheric water harvesting: The role of machine learning techniques, *Coord. Chem. Rev.*, 2026, **548**, 217211.

42 I. E. Collings and A. L. Goodwin, Metal–organic frameworks under pressure, *J. Appl. Phys.*, 2019, **126**, 181101.

43 K. Roztocki, S. Sobczak, A. Smaruj, A. Walczak, M. Gołdyn, V. Bon, S. Kaskel and A. R. Stefankiewicz, *J. Mater. Chem. A*, 2023, **11**, 18646–18650.

44 C. Serre, S. Bourrelly, A. Vimont, N. A. Ramsahye, G. Maurin, P. L. Llewellyn, M. Daturi, Y. Filinchuk, O. Leynaud, P. Barnes and G. Férey, An Explanation for the Very Large Breathing Effect of a Metal–Organic Framework during CO_2 Adsorption, *Adv. Mater.*, 2007, **19**, 2246–2251.

45 A. V. Dotsenko, L. B. Glebov and V. A. Tsekhomsky, *Physics and Chemistry of Photochromic Glasses*, CRC Press, Boca Raton, 1997.

46 Z. Xiong, W. Gong, P. Xu, M. Jiang, X. Cai, Y. Zhu, X. Ping, H. Feng, H. Ma and Z. Qian, Reexamining the heavy-atom-effect: The universal heavy-atom-induced fluorescence enhancement principle for through-space conjugated AIEgens, *Chem. Eng. J.*, 2023, **451**, 139030.

47 J. M. Crowley, J. Tahir-Kheli and W. A. Goddard, Resolution of the Band Gap Prediction Problem for Materials Design, *J. Phys. Chem. Lett.*, 2016, **7**, 1198–1203.

48 Y. Zhang, X. Wang, K. Xu, F. Zhai, J. Shu, Y. Tao, J. Wang, L. Jiang, L. Yang, Y. Wang, W. Liu, J. Su, Z. Chai and S. Wang, Near-Unity Energy Transfer from Uranyl to Europium in a Heterobimetallic Organic Framework with Record-Breaking Quantum Yield, *J. Am. Chem. Soc.*, 2023, **145**, 13161–13168.

49 O. Pajuelo-Corral, L. Razquin-Bobillo, S. Rojas, J. A. J. A. García, D. Choquesillo-Lazarte, A. Salinas-Castillo, R. Hernández, A. Rodríguez-Diéguez, J. Cepeda and S. Ochoa, Lanthanide(III) Ions and 5-Methylisophthalate Ligand Based Coordination Polymers: An Insight into Their Photoluminescence Emission and Chemosensing for Nitroaromatic Molecules, *Nanomaterials*, 2022, **12**, 3977.

50 M. X. Hong, C. Chen, L. Cao, J. Zheng and X. Y. Zheng, Highly Stable Lanthanide Cluster-Based Luminescent Materials Constructed from β-Diketone to 1,10-Phenanthroline Exhibiting Ultrahigh Photoluminescence and Efficient Pesticide Detection, *J. Mater. Chem. C*, 2023, **11**, 16125–16134.

51 M. H. V. Werts, R. T. F. Jukes and J. W. Verhoeven, The Emission Spectrum and the Radiative Lifetime of Eu^{3+} in Luminescent Lanthanide Complexes, *Phys. Chem. Chem. Phys.*, 2002, **4**, 1542–1548.

52 J. D. L. Dutra, T. D. Bispo and R. O. Freire, LUMPAC Lanthanide Luminescence Software: Efficient and User Friendly, *J. Comput. Chem.*, 2014, **35**, 772–775.

53 M. Latva, H. Takalob, V. M. Mukkala, C. Matachescu, J. C. Rodríguez-Ubis and J. Kankare, Correlation between the Lowest Triplet State Energy Level of the Ligand and Lanthanide(III) Luminescence Quantum Yield, *J. Lumin.*, 1997, **75**, 149–169.

54 M. Hasegawa, H. Ohmagari, H. Tanaka and K. Machida, Luminescence of Lanthanide Complexes: From Fundamental to Prospective Approaches Related to Water- and Molecular-Stimuli, *J. Photochem. Photobiol., C*, 2022, **50**, 100484.

55 E. Cavalli, S. Ruggieri, S. Mizzoni, C. Nardon, M. Bettinelli and F. Piccinelli, NIR-emission from Yb(III)- and Nd(III)-based complexes in the solid state sensitized by a ligand system absorbing in a broad UV and visible spectral window, *Results Chem.*, 2022, **4**, 100388.

56 C. Jiang and P. Song, *Nonlinear-Emission Photonic Glass Fiber and Waveguide Devices*, Cambridge University Press, Cambridge, 2019.

57 S. V. Camyshan, N. P. Gritsan, V. V. Korolev and N. M. Bazhin, Quenching of the Luminescence of Organic Compounds by Oxygen in Glassy Matrices, *Chem. Phys.*, 1990, **142**, 59–68.

58 J. R. Lakowicz and G. Weber, Quenching of Fluorescence by Oxygen. A Probe for Structural Fluctuations in Macromolecules, *Biochemistry*, 1973, **12**, 4161.

59 K. Binnemans, Interpretation of Europium(III) Spectra, *Coord. Chem. Rev.*, 2015, **295**, 1–45.

60 A. Beeby, I. M. Clarkson, R. S. Dickins, S. Faulkner, D. Parker, L. Royle, A. S. de Sousa, J. A. Gareth Williams and M. Woods, Non-Radiative Deactivation of the Excited States of Europium, Terbium and Ytterbium Complexes by Proximate Energy-Matched OH, NH and CH Oscillators: An Improved Luminescence Method for Establishing Solution Hydration States, *J. Chem. Soc., Perkin Trans. 2*, 1999, 493–504.

61 A. Monguzzi, A. Milani, L. Lodi, M. I. Trioni, R. Tubino and C. Castiglioni, Vibrational Overtones Quenching of near Infrared Emission in Er^{3+} Complexes, *New J. Chem.*, 2009, **33**, 1542–1548.

62 Z. Chen and H. Xu, in *Rare Earth Coordination Chemistry: Fundamentals and Applications*, ed. C. Huang, Wiley, Singapore, 2010.

63 T. Zhang, X. Zhu, C. C. W. Cheng, W. M. Kwok, H. L. Tam, J. Hao, D. W. J. Kwong, W. K. Wong and K. L. Wong, Water-Soluble Mitochondria-Specific Ytterbium Complex with Impressive NIR Emission, Water-Soluble Mitochondria-Specific Ytterbium Complex with Impressive NIR Emission, *J. Am. Chem. Soc.*, 2011, **133**, 20120–20122.

64 M. C. Burla, R. Caliandro, M. Camalli, B. Carrozzini, G. L. Cascarano, C. Giacovazzo, M. Mallamo, A. Mazzone, G. Polidori and R. Spagna, SIR2011: A New Package for Crystal Structure Determination and Refinement, *J. Appl. Crystallogr.*, 2012, **45**, 357–361.

65 O. V. Dolomanov, L. J. Bourhis, R. J. Gildea, J. A. K. K. Howard and H. Puschmann, OLEX2: A Complete Structure Solution, Refinement and Analysis Program, *J. Appl. Crystallogr.*, 2009, **42**, 339–341.

66 M. J. Frisch, G. W. Trucks, H. B. Schlegel, G. E. Scuseria, M. A. Robb, J. R. Cheeseman, G. Scalmani, V. Barone, G. A. Petersson, H. Nakatsuji, X. Li, M. Caricato, A. V. Marenich, J. Bloino, B. G. Janesko, R. Gomperts, B. Mennucci, H. P. Hratchian, J. V. Ortiz, A. F. Izmaylov, J. L. Sonnenberg, D. Williams-Young, F. Ding, F. Lipparini, F. Egidi, J. Goings, B. Peng, A. Petrone, T. Henderson, D. Ranasinghe, V. G. Zakrzewski, J. Gao, N. Rega, G. Zheng, W. Liang, M. Hada, M. Ehara, K. Toyota, R. Fukuda, J. Hasegawa, M. Ishida, T. Nakajima, Y. Honda, O. Kitao, H. Nakai, T. Vreven, K. Throssell, J. A. Montgomery Jr., J. E. Peralta, F. Ogliaro, M. J. Bearpark, J. J. Heyd, E. N. Brothers, K. N. Kudin, V. N. Staroverov, T. A. Keith, R. Kobayashi, J. Normand, K. Raghavachari, A. P. Rendell, J. C. Burant, S. S. Iyengar, J. Tomasi, M. Cossi, J. M. Millam, M. Klene, C. Adamo, R. Cammi, J. W. Ochterski, R. L. Martin, K. Morokuma, O. Farkas, J. B. Foresman and D. J. Fox, *Gaussian 16 Revision C.01*, 2016.

67 F. Weigend and R. Ahlrichs, Balanced basis sets of split valence, triple zeta valence and quadruple zeta valence quality for H to Rn: Design and assessment of accuracy, *Phys. Chem. Chem. Phys.*, 2005, **7**, 3297–3305.

68 F. Neese, Software update: The ORCA program system---Version 5.0, *Wiley Interdiscip. Rev.: Comput. Mol. Sci.*, 2022, **12**, e1606.

69 S. Grimme, J. Antony, S. Ehrlich and H. Krieg, A consistent and accurate ab initio parametrization of density functional dispersion correction (DFT-D) for the 94 elements H-Pu, *J. Chem. Phys.*, 2010, **132**, 154104.

70 A. Tkatchenko and M. Scheffler, Accurate Molecular van der Waals Interactions from Ground-State Electron Density and Free-Atom Reference Data, *Phys. Rev. Lett.*, 2009, **102**, 073005.

71 J. P. Perdew, K. Burke and M. Ernzerhof, Generalized Gradient Approximation Made Simple, *Phys. Rev. Lett.*, 1996, **77**, 3865.

72 (*a*) CCDC 2456148: Experimental Crystal Structure Determination, 2026, DOI: **10.5517/ccdc.csd.cc2nftlj**; (*b*) CCDC 2456149: Experimental Crystal Structure Determination, 2026, DOI: **10.5517/ccdc.csd.cc2nftmk**; (*c*) CCDC 2456150: Experimental Crystal Structure Determination, 2026, DOI: **10.5517/ccdc.csd.cc2nftnl**; (*d*) CCDC 2456151: Experimental Crystal Structure Determination, 2026, DOI: **10.5517/ccdc.csd.cc2nftpm**; (*e*) CCDC 2456152: Experimental Crystal Structure Determination, 2026, DOI: **10.5517/ccdc.csd.cc2nftqn**; (*f*) CCDC 2456153: Experimental Crystal Structure Determination, 2026, DOI: **10.5517/ccdc.csd.cc2nftrp**.